Supporting Information

Tetravalent organic cation-enabled dual interfacial regulation for durable aqueous zinc–iodine batteries

Doudou Feng[1], Yanchun Xie[2], Yinlin Shen[1], Hao Zhang[1], Xuan Chen[2], Peng-Fei Wang[3], Jiaqian Qin[4], Yucong Jiao[2,*], and Jijian Xu[1,5*]

[1]*Department of Chemistry, City University of Hong Kong, Hong Kong, 999077, China.*

[2]*College of Chemistry and Chemical Engineering, Donghua University, Shanghai 201620, China.*

[3]*Center of Nanomaterials for Renewable Energy, State Key Laboratory of Electrical Insulation and Power Equipment, School of Electrical Engineering, Xi'an Jiaotong University, Xi'an 710049, Shaanxi, China.*

[4]*Center of Excellence on Advanced Materials for Energy Storage, Department of Materials Science, Faculty of Science, Chulalongkorn University, Bangkok 10330, Thailand.*

[5]*Shenzhen Research Institute, City University of Hong Kong, Shenzhen, 518057, China.*

Correspondence should be addressed to Y.C.J. (email: yucong.jiao@dhu.edu.cn), and J.J.X. (email: jijianxu@cityu.edu.hk)

This file includes

Suppl. Fig. 1. Molecular structures of DAAOTF and $OTA(OTF)_4$ S5

Suppl. Fig. 2. NMR spectra of DAACl and DAAOTF S5

Suppl. Fig. 3. NMR spectra of $OTABr_4$ and $OTA(OTF)_4$ S5

Suppl. Fig. 4. LC and HRMS for $OTA(OTF)_4$ S6

Suppl. Fig. 5. N 1s XPS patterns of $OTA(OTF)_4$ S6

Suppl. Fig. 6. Photograph of batch-prepared HVOC S6

Suppl. Fig. 7. MESP maps of I^-, I_2, I_3^- and I_5^- S7

Suppl. Fig. 8. Energy level diagrams S7

Suppl. Fig. 9. Energy gaps S7

Suppl. Fig. 10. Charge density difference maps for HVOC complexes with I^- S8

Suppl. Fig. 11. UV–Vis absorption spectra S8

Suppl. Fig. 12. N 1s XPS patterns of HVOC and HVOC&@ I_3^- S8

Suppl. Fig. 13. MD simulated EDL configuration near the Zn electrode with MVOC S9

Suppl. Fig. 14. Corresponding cumulated density distributions of water molecules S9

Suppl. Fig. 15. MD simulated EDL configuration during charing S9

Suppl. Fig. 16. Energy level diagrams and energy gaps S10

Suppl. Fig. 17. Raman spectra of H_2O, BE, and HVOC electrolytes S10

Suppl. Fig. 18. Zeta potentials S10

Suppl. Fig. 19. Calculated *log P* values S11

Suppl. Fig. 20. The schematical illustration of solvation structure S11

Suppl. Fig. 21. Calculated binding energies and MD resultes S12

Suppl. Fig. 22. NMR spectra of H_2O and different electrolytes S12

Suppl. Fig. 23. Raman spectra of BE and HVOC electrolytes S13

Suppl. Fig. 24. Calculated reduction potentials by DFT S13

Suppl. Fig. 25. Corresponding EXAFS spectra in *R* space S14

Suppl. Fig. 26. Wavelet transformation of Zn *k*-edge for Zn foil and BE S14

Suppl. Fig. 27. LF NMR spectra of H_2O and different electrolytes. S14

Suppl. Fig. 28. C 1s XPS fitting spectra. S15

Suppl. Fig. 29. The ionic conductivity and binding energies results S15

Suppl. Fig. 30. The band gap energy and average Young's modulus. S16

Suppl. Fig. 31. Sputtering depth profiles of $C_2H_4N^+$ at the I_2 electrode. S16

Suppl. Fig. 32. Sputtering depth profiles of $C_2H_4N^+$ at the Zn electrode S17

Suppl. Fig. 33. Sputtering depth profiles of ZnF^- at the Zn electrode S17

Suppl. Fig. 34. Sputtering depth profiles of ZnS^- at the Zn electrode S17

Suppl. Fig. 35. 2D element distribution map after cycling with HVOC S18

Suppl. Fig. 36. 2D element distribution map after cycling with BE S18

Suppl. Fig. 37. CV curves of Zn||I_2 batteries S19

Suppl. Fig. 38. GITT curves and the corresponding Zn^{2+} diffusion coefficients S19

Suppl. Fig. 39. In-situ Raman spectra at the range of 2800-3800 cm^{-1} S20

Suppl. Fig. 40. The fitted Raman spectra in HVOC systems S21

Suppl. Fig. 41. The fitted Raman spectra in BE systems S21

Suppl. Fig. 42. The calculated HBs area ratios S22

Suppl. Fig. 43. In-situ Raman spectra at the range of 980-1280 cm^{-1} S22

Suppl. Fig. 44. Electrochemical stability window of different electrolytes S22

Suppl. Fig. 45. Tafel curves for different electrolytes S23

Suppl. Fig. 46. CA curves and fitted I_{dl}, I_{2D}, and I_{3D} contribution S23

Suppl. Fig. 47. SEM images for nucleation characterization S24

Suppl. Fig. 48. In situ EIS curves of the Zn||Zn batteries S25

Suppl. Fig. 49. The calculated of E_a for different electrolytes S25

Suppl. Fig. 50. Long-term cycling stability of Zn||Cu cells S25

Suppl. Fig. 51. Performance at different $Zn(OTF)_2$ concentration S26

Suppl. Fig. 52. Long-term cycling stability of Zn||Cu cells with 0.15 m HVOC S27

Suppl. Fig. 53. Long-term cycling stability of Zn||Zn cells with different electrolytes S27

Suppl. Fig. 54. Long-term cycling stability of Zn||Zn cells with HVOC S28

Suppl. Fig. 55. Cycling stability pure YP50 electrode with HVOC S28

Suppl. Fig. 56. Cycling stability of Zn||I_2 battery with HVOC at 0.2 A g^{-1} S28

Suppl. Fig. 57. Cycling stability of Zn||I_2 battery with HVOC at 1 A g^{-1} S29

Suppl. Fig. 58. Cycling stability of Zn||I_2 battery with HVOC S29

Suppl. Fig. 59. The SEM images of Zn electrode S29

Suppl. Fig. 60. Characteristion for HVOC electrolytes S30

Suppl. Fig. 61. Cycling stability of Zn||I_2 battery with different HVOC concentrations S30

Suppl. Fig. 62. Performance of Zn||I_2 battery with HVOC from 25 ºC to –40 ºC S31

Suppl. Fig. 63. Cycling performance of Zn||I_2 battery with HVOC at 60 ºC S31

Suppl. Fig. 64. Performance of HVOC in $ZnSO_4$ based electrolytes S32

Suppl. Fig. 65. Optical photographs of different electrolytes at −40 °C S33

Suppl. Fig. 66. Characteristion for Spy^+ and Dpy^{2+} S33

Suppl. Fig. 67. Performance of Spy^+ and Dpy^{2+} in $Zn(OTF)_2$ based electrolytes S34

Suppl. Fig. 68. Performance of Spy^+ and Dpy^{2+} in $ZnSO_4$ based electrolytes S35

Suppl. Table 1 The parameter of the 0.14 Ah pouch cell S36

Suppl. Table 2 Comparison of the Zn||I_2 battery performance S37

Suppl. Table 3 Simulated electrolyte compositions S38

Suppl. Table 4 The fitted EIS results with BE S39

Suppl. Table 5 The fitted EIS results with HVOC S39

Supplementary References S40

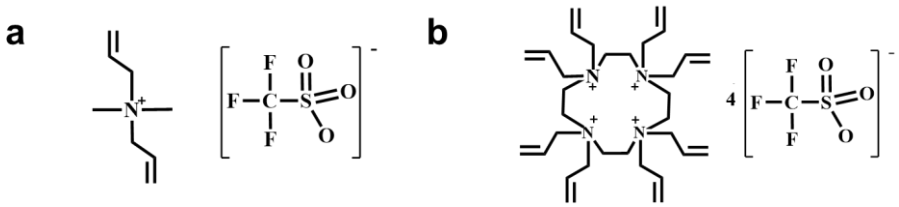

Supplementary Fig. 1 Molecular structures of **a** DAAOTF and **b** $OTA(OTF)_4$.

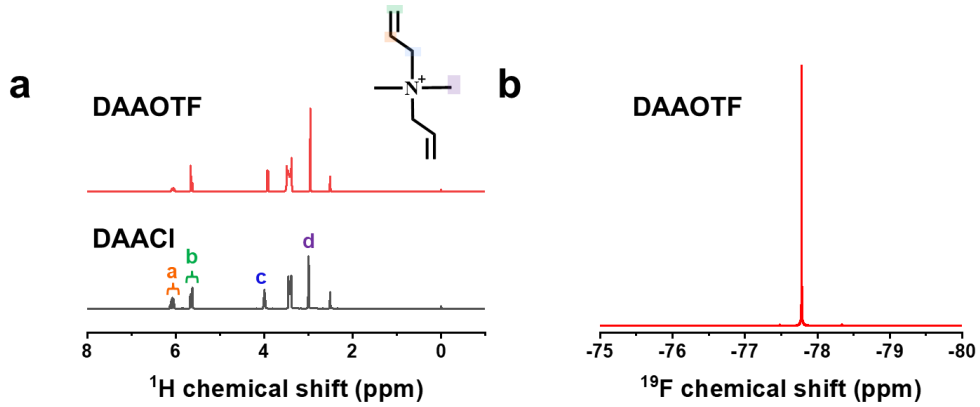

Supplementary Fig. 2 **a** ^{1}H NMR spectra of DAACl and DAAOTF. **b** ^{19}F NMR spectrum of DAAOTF.

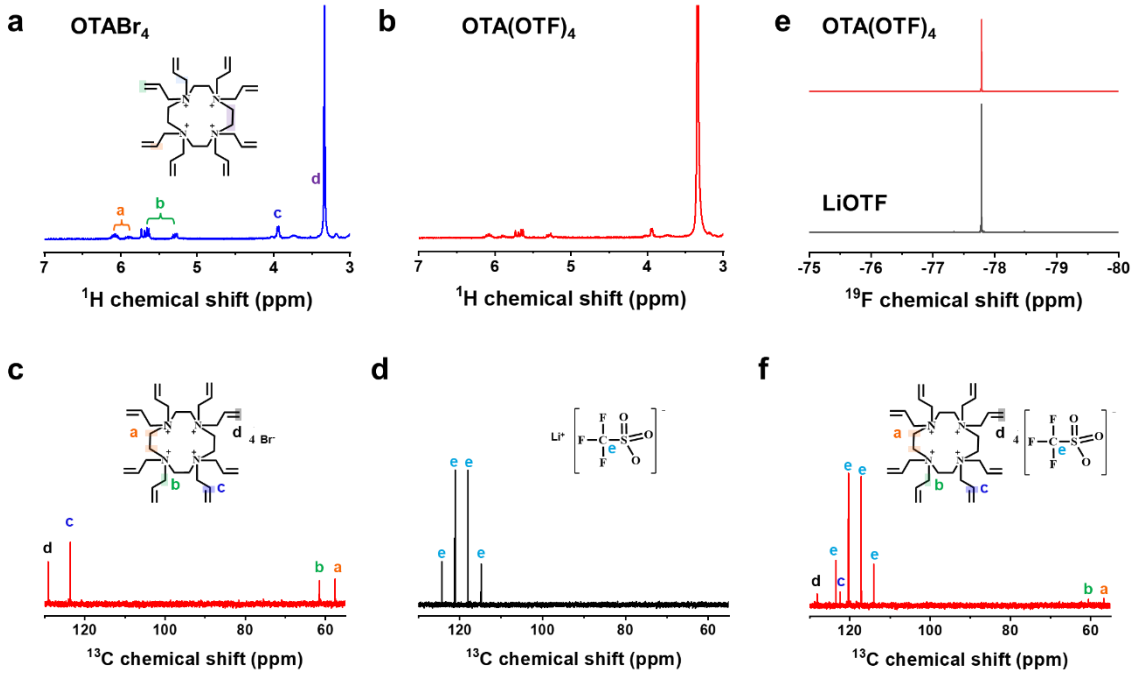

Supplementary Fig. 3 ^{1}H NMR spectra of **a** $OTABr_4$ and **b** $OTA(OTF)_4$. ^{13}C NMR spectra of **c** $OTABr_4$ and **d** LiOTF. **e** ^{19}F NMR spectra of LiOTF and $OTA(OTF)_4$. **f** ^{13}C NMR spectra of $OTA(OTF)_4$

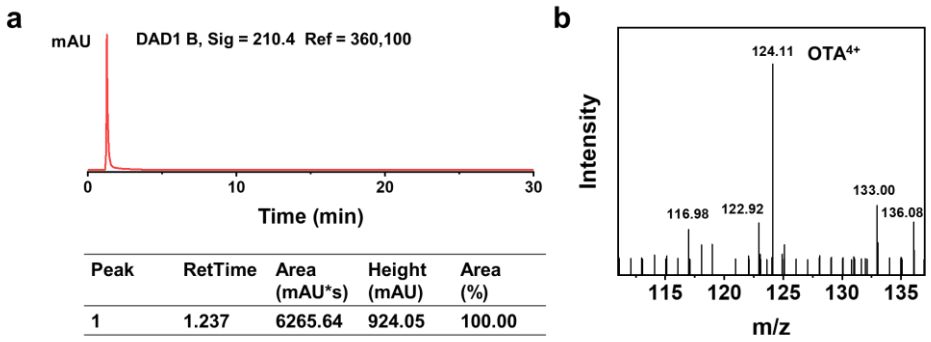

Peak	RetTime	Area (mAU*s)	Height (mAU)	Area (%)
1	1.237	6265.64	924.05	100.00

Supplementary Fig. 4 a Liquid chromatography and **b** high-resolution mass spectrometry for $OTA(OTF)_4$.

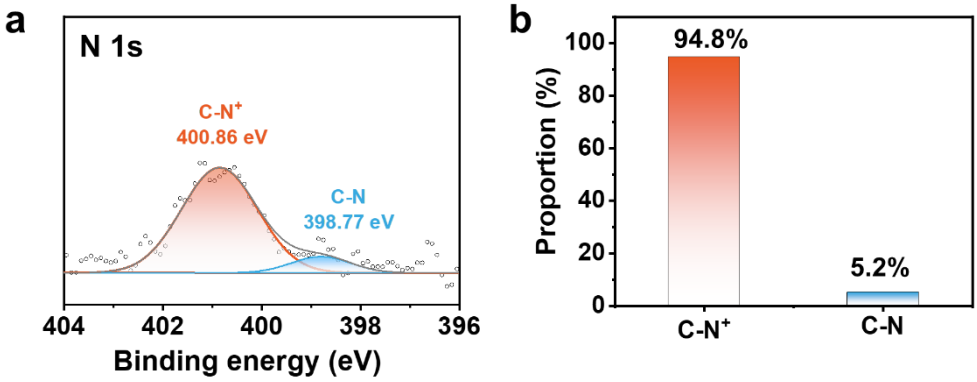

Supplementary Fig. 5 a N 1s XPS patterns of $OTA(OTF)_4$ and **b** the corresponding calculated proportion of $C–N^+$ and C–N components.

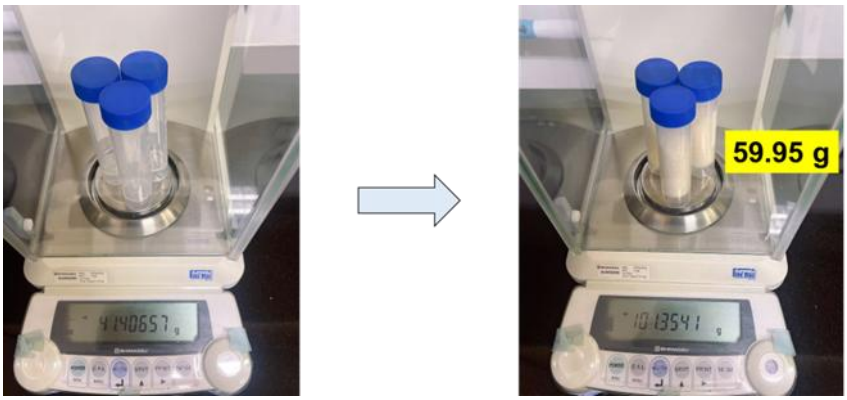

Supplementary Fig. 6 Photograph of batch-prepared HVOC-containing $OTA(OTF)_4$.

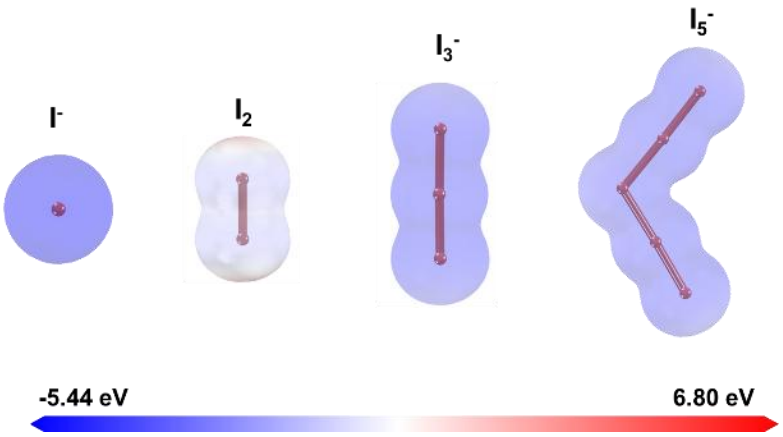

Supplementary Fig. 7 MESP maps of I^-, I_2, I_3^- and I_5^-.

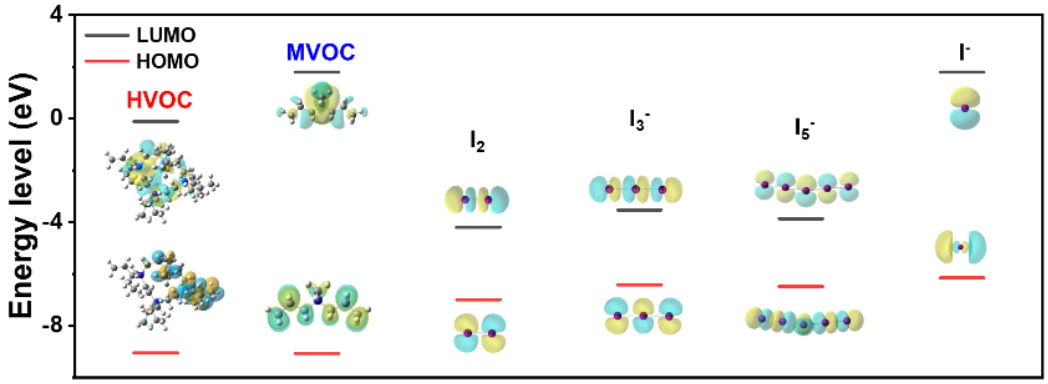

Supplementary Fig. 8 Energy level diagrams showing the LUMO and HOMO of HVOC, MVOC, I_2, I_3^-, I_5^- and I^-.

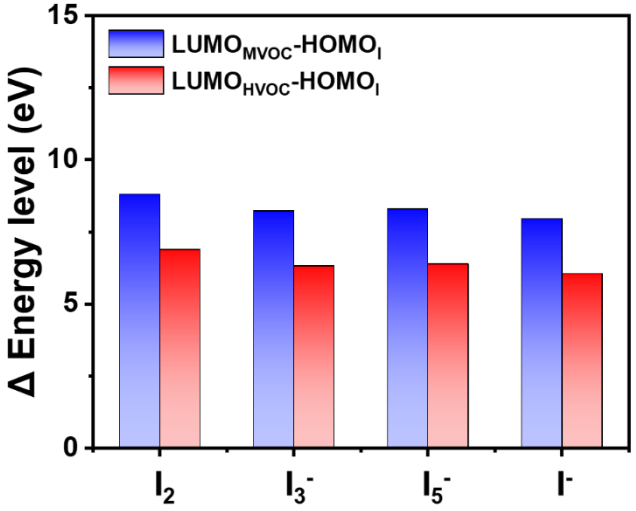

Supplementary Fig.9 Energy gaps between the LUMO of MVOC and HVOC and the HOMO of iodine species.

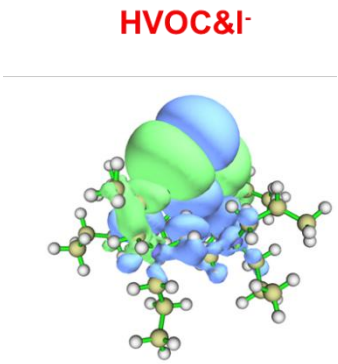

Supplementary Fig. 10 Charge density difference maps for HVOC complexes with I^-.

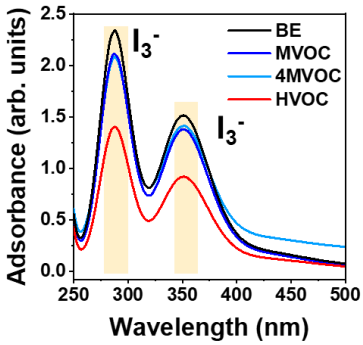

Supplementary Fig. 11 UV–Vis absorption spectra of polyiodide retention experiments in various electrolytes at 0 h.

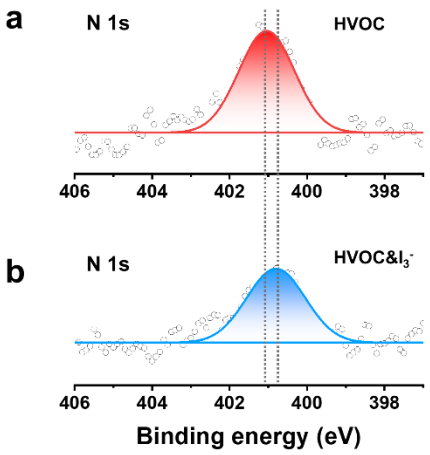

Supplementary Fig. 12 N 1s XPS patterns of **a** HVOC and **b** HVOC&@ I_3^-.

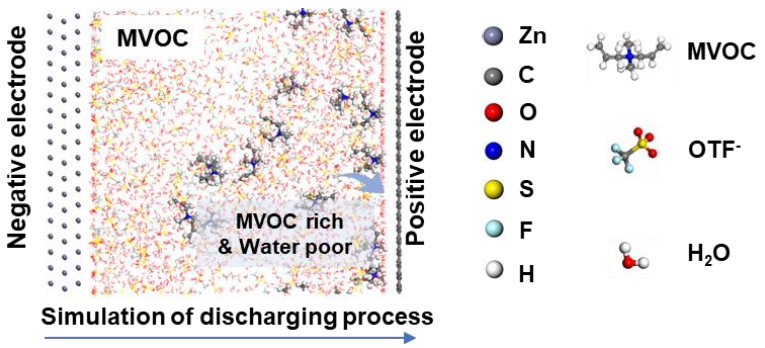

Supplementary Fig. 13 MD simulated EDL configuration near the I_2 electrode and Zn electrode with MVOC.

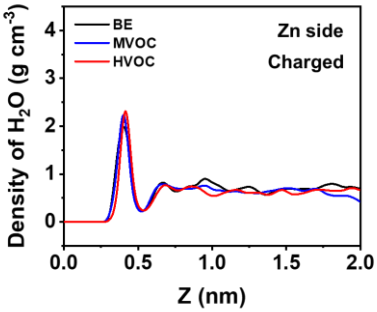

Supplementary Fig. 14 Corresponding cumulated density distributions of water molecules near charged Zn electrode in different electrolytes.

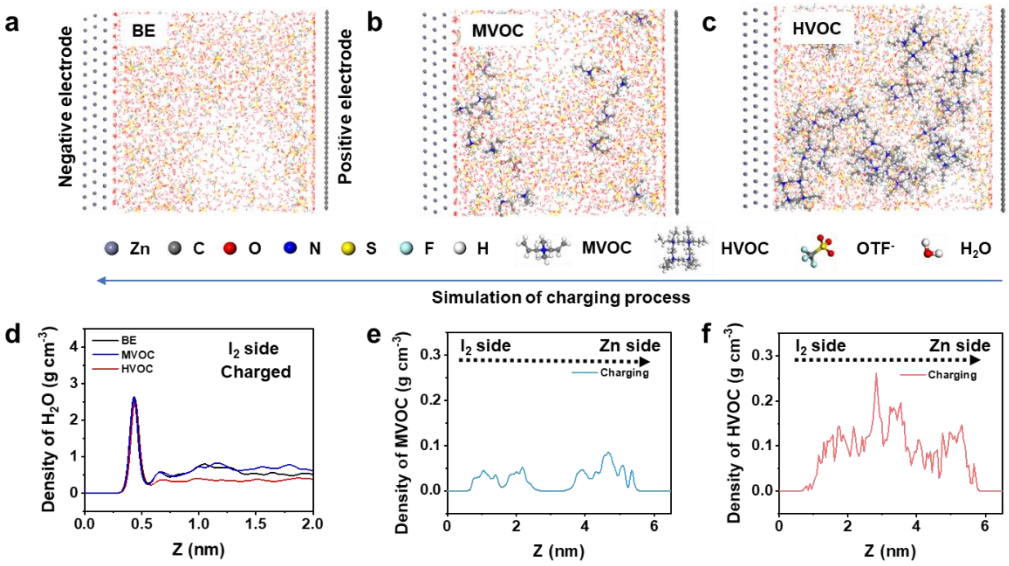

Supplementary Fig. 15 MD simulated EDL configuration near the I_2 electrode and Zn electrode with **a** BE, **b** MVOC and **c** HVOC during charging. **d** Corresponding cumulated density distributions of water molecules near charged I_2 electrode in different electrolytes. **e** Corresponding cumulated density distributions of MVOC in MVOC electrolyte. **f** Corresponding cumulated density distributions of HVOC in HVOC electrolyte.

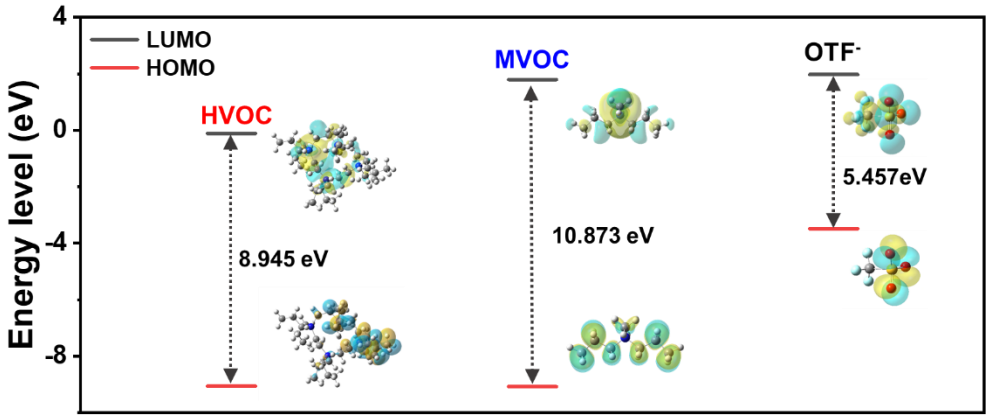

Supplementary Fig. 16 Energy level diagrams showing the LUMO and HOMO of HVOC, MVOC, and OTF^- and their corresponding energy gaps.

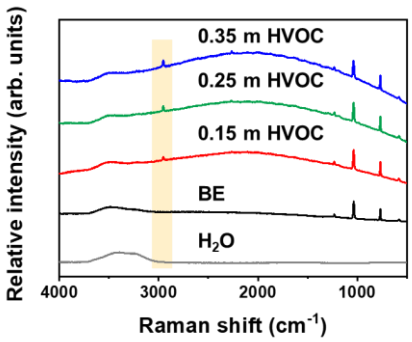

Supplementary Fig. 17 Raman spectra of H_2O, BE, and electrolytes with different concentrations of HVOC.

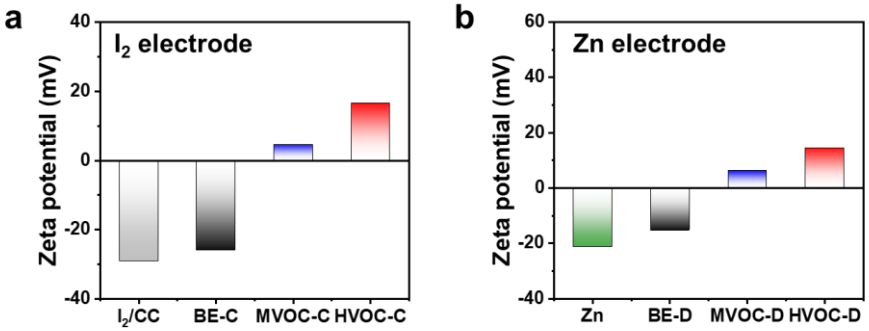

Supplementary Fig. 18 Zeta potentials of the **a** charged (C) I_2 electrode, and **b** discharged (D) Zn electrode, comparing different electrolytes.

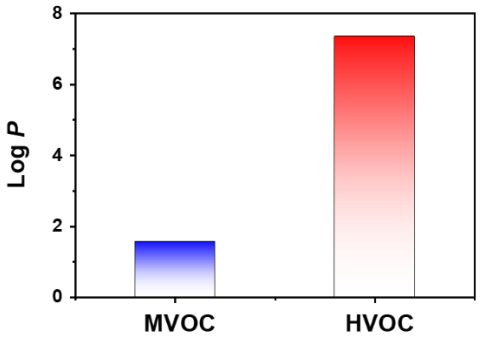

Supplementary Fig. 19 Calculated *log P* values of MVOC and HVOC.

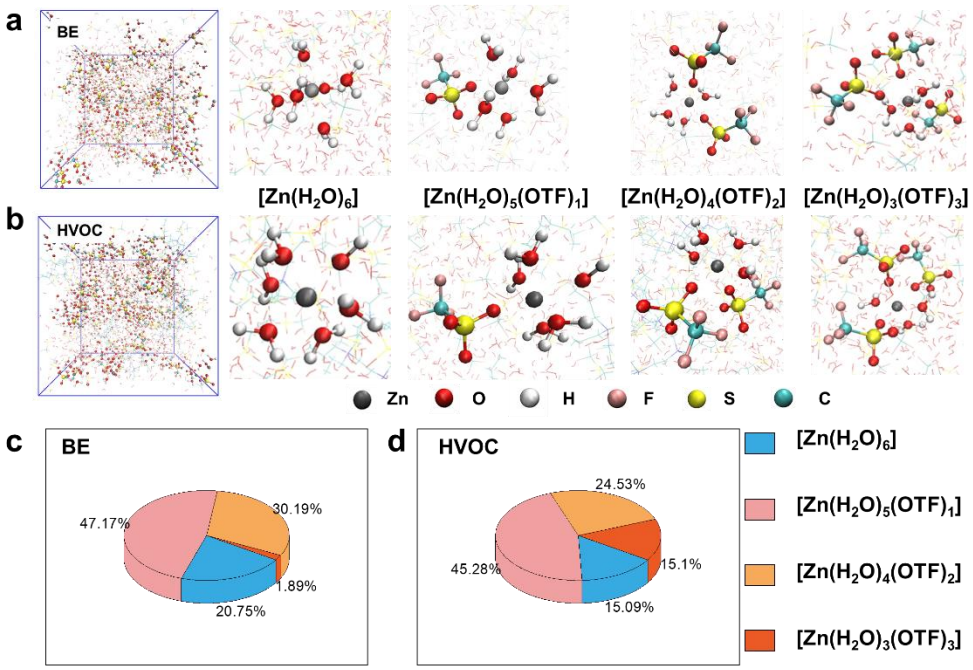

Supplementary Fig. 20 The schematical illustration of solvation structure in **a** BE and **b** HVOC electrolytes. The calculated specific solvation structure ratio in **c** BE and **d** HVOC electrolytes.

Supplementary Note 1 Beyond average coordination statistics, we further analyzed the specific solvation structure surrounding Zn^{2+}. In BE, the Zn^{2+} solvation structure is dominated by $[Zn(H_2O)_6]$ (20.75%), $[Zn(H_2O)_5(OTF)_1]$ (47.17%), and $[Zn(H_2O)_4(OTF)_2]$ (30.19%), with only 1.89% of $[Zn(H_2O)_3(OTF)_3]$ species. In contrast, HVOC induces a significant redistribution of these motifs, most notably increasing the fraction of $[Zn(H_2O)_3(OTF)_3]$ to 15.1%. The fraction of $[Zn(H_2O)_6]$, $[Zn(H_2O)_5(OTF)_1]$, and $[Zn(H_2O)_4(OTF)_2]$ is 15.09%, 45.28%, and 24.53% respectively.

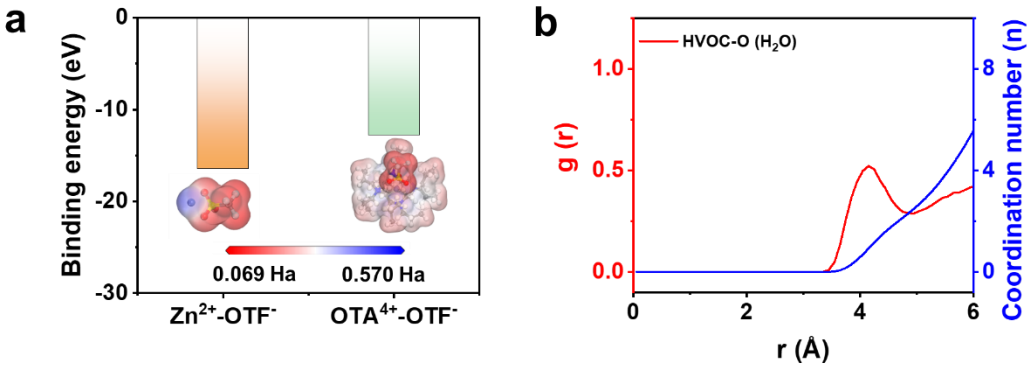

Supplementary Fig. 21 a Calculated binding energies of Zn^{2+}–OTF^- and HVOC–OTF^-. **b** RDF results for HVOC–O (H_2O) obtained from MD simulations in HVOC electrolyte.

Supplementary Note 2 The calculated binding energy of the Zn^{2+}–OTF^- is larger that of the OTA^{4+}–OTF^-, indicating that OTF^- preferentially coordinates with Zn^{2+} rather than with HVOC. This preference can be understood by considering ionic size and steric factors. OTF^- is a bulky anion, whereas Zn^{2+} possesses a small ionic radius and a highly localized charge distribution, allowing OTF^- to approach Zn^{2+} with relatively low steric hindrance. In contrast, OTA^{4+} has a substantially larger molecular framework, and steric repulsion limits its ability to engage OTF^- despite its high formal charge. The MD simulations further reveal that HVOC interacts with surrounding water molecules, reducing the number of water molecules available for Zn^{2+} solvation. This decrease in Zn^{2+}–H_2O interactions increases the competitiveness of OTF^- to enter the Zn^{2+} primary solvation shell.

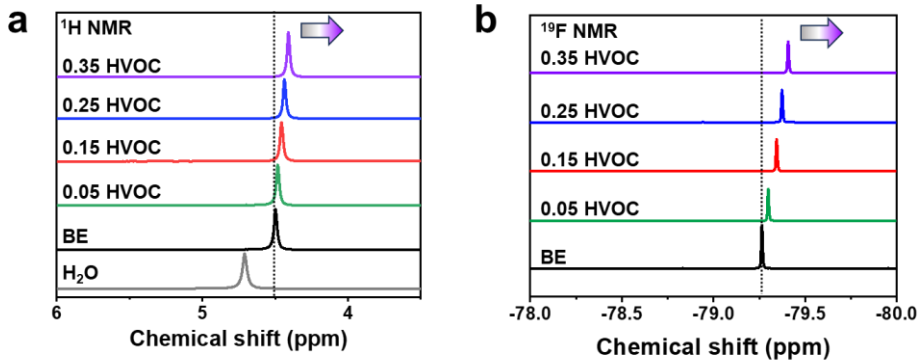

Supplementary Fig. 22 a ^1H NMR and **b** ^{19}F NMR spectra of H_2O and different electrolytes.

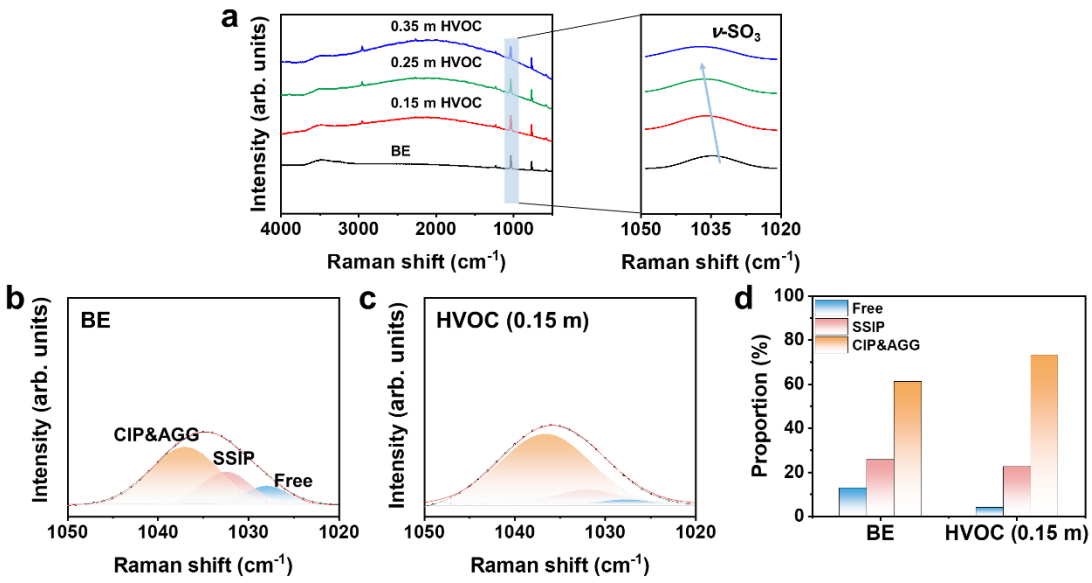

Supplementary Fig. 23 a Raman spectra of BE and electrolytes with different concentrations of HVOC. The fitted Raman spectra of **b** BE and **c** HVOC (0.15 m). **d** The calculated Free anion, SSIP and CIP&AGG area ratios.

Supplementary Note 3 In the 1020–1050 cm^{-1} region associated with the ν-SO_3 stretching of OTF^-, peak deconvolution allows us to distinguish free OTF^-(~1028 cm^{-1}), solvent-separated ion pairs (SSIP, ~1032 cm^{-1}), contact ion pairs and aggregates (CIP&AGG, ~1037 cm^{-1})[1].

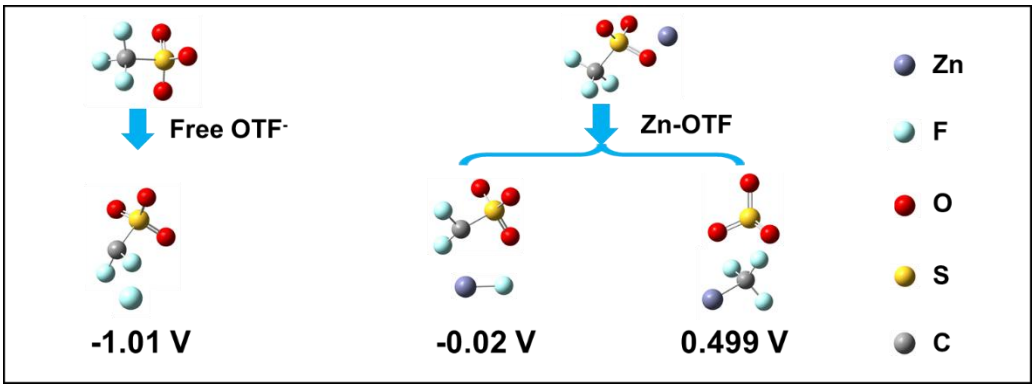

Supplementary Fig. 24 Calculated reduction potentials by DFT.

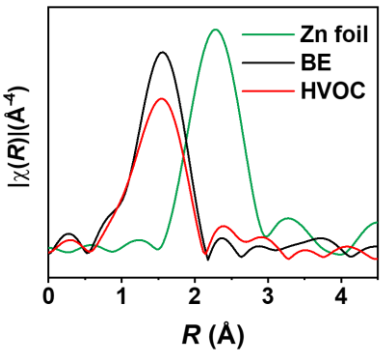

Supplementary Fig. 25 Corresponding EXAFS spectra in *R* space, revealing local Zn coordination environments.

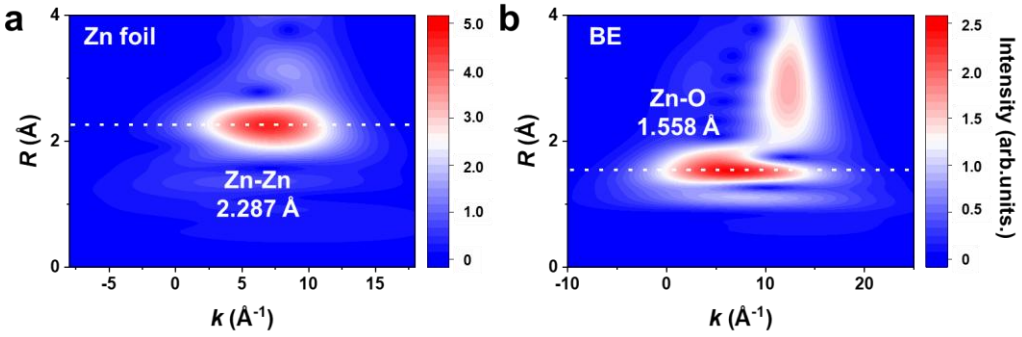

Supplementary Fig. 26 Wavelet transformation of Zn *k*-edge for **a** Zn foil and **b** BE.

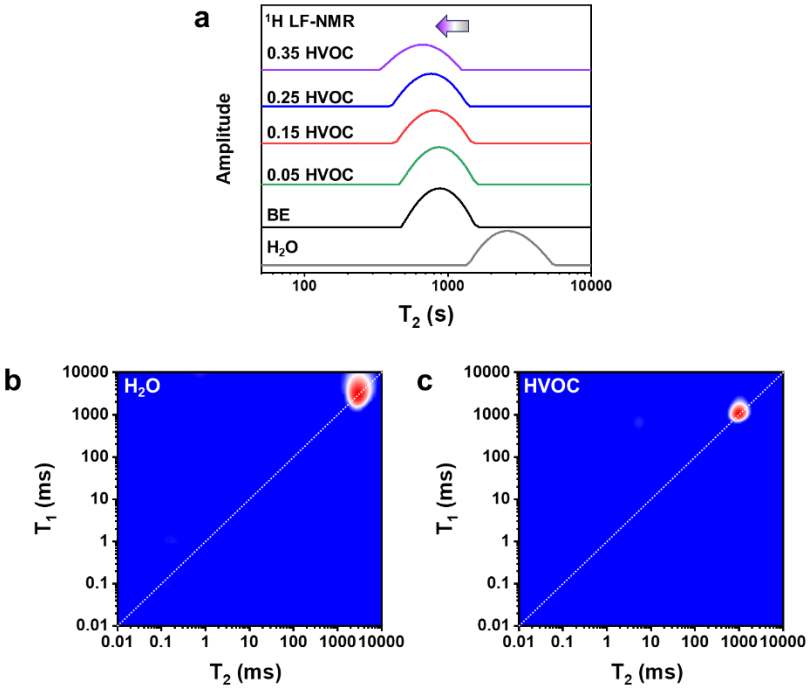

Supplementary Fig. 27 a ^{1}H LF-NMR spectra of H_2O and different electrolytes. Superimposed 2D LF ^{1}H T_1–T_2 mapping of **b** H_2O and **c** HVOC.

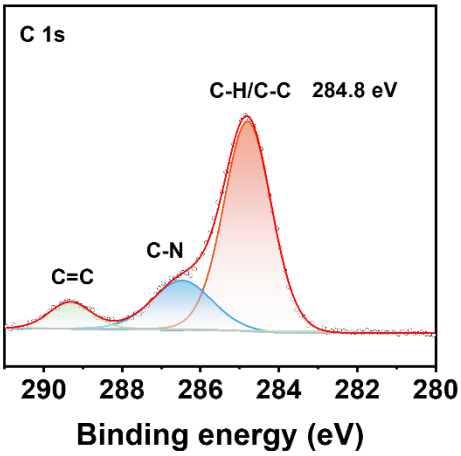

Supplementary Fig. 28 The C 1s XPS fitting spectra.

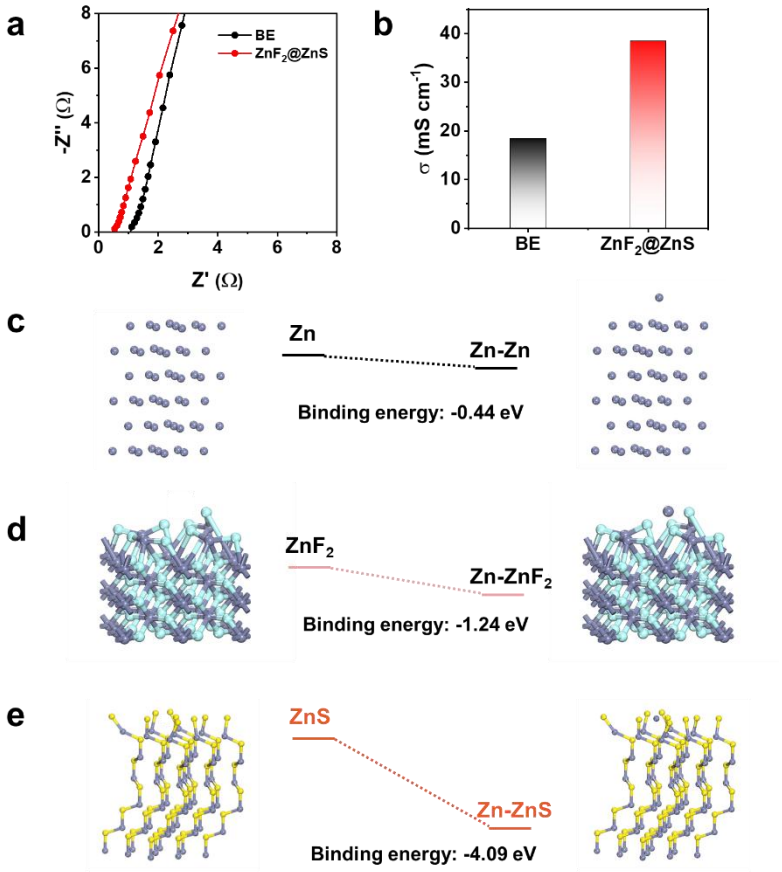

Supplementary Fig. 29 a The A. C. impedance spectra and **b** the corresponding ionic conductivity (σ) of BE and ZnF_2@ZnS. The binding energy of **c** Zn metal, **d** ZnF_2 and **e** ZnS.

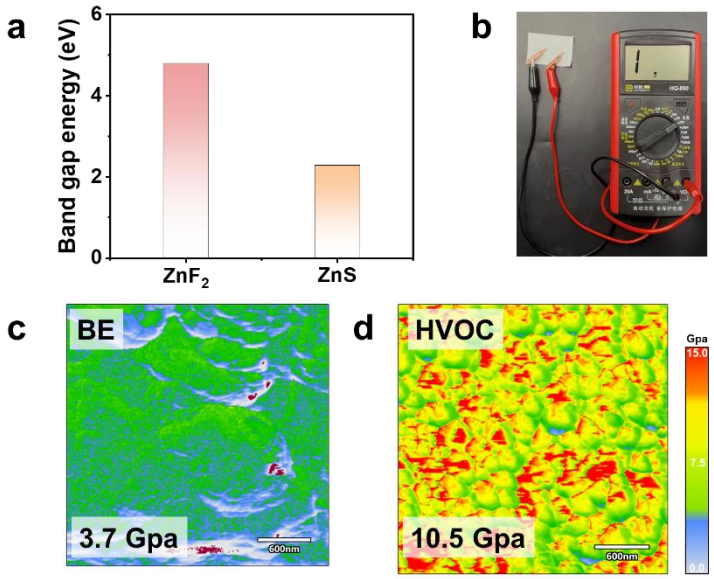

Supplementary Fig. 30 a The band gap energy of the ZnF_2 and ZnS. **b** Multimeter measurement of the surface resistance of the Zn electrode coated with ZnF_2/ZnS. The average Young's modulus of the cycled Zn electrode in **c** BE and **d** HVOC.

Supplementary Note 4 The calculated band gap energies are 4.8 eV for ZnF_2 and 2.28 eV for ZnS, characteristic of an insulating phase and a wide-band-gap semiconductor, respectively, and therefore far less electronically conductive than metallic Zn. Consistently, direct resistance measurements of Zn electrodes coated with ZnF_2 or ZnS show resistances exceeding the instrumental detection limit, confirming that these SEI components act as electronically blocking layers.

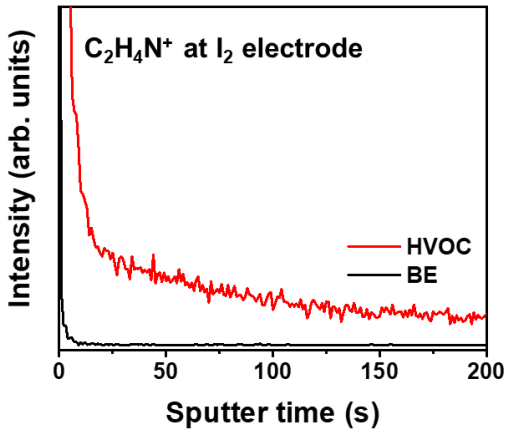

Supplementary Fig. 31 Sputtering depth profiles of $C_2H_4N^+$ at the I_2 electrode with different electrolytes.

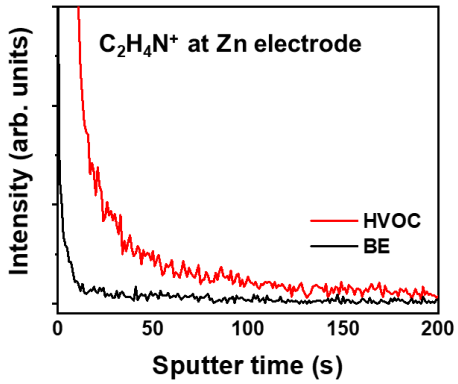

Supplementary Fig. 32 Sputtering depth profiles of $C_2H_4N^+$ at the Zn electrode with different electrolytes.

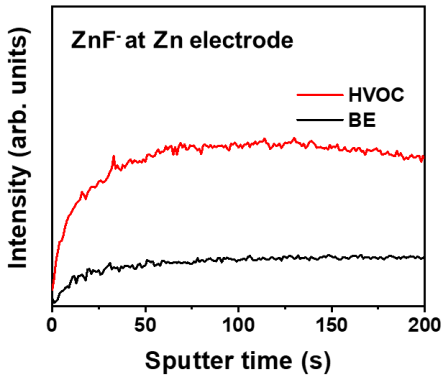

Supplementary Fig. 33 Sputtering depth profiles of ZnF^- at the Zn electrode with different electrolytes.

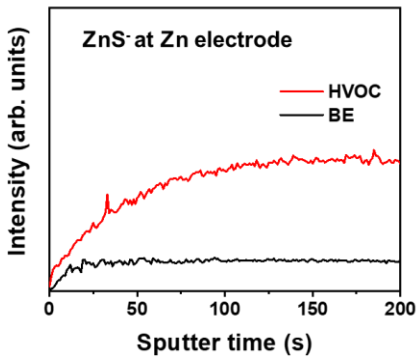

Supplementary Fig. 34 Sputtering depth profiles of ZnS^- at the Zn electrode with different electrolytes.

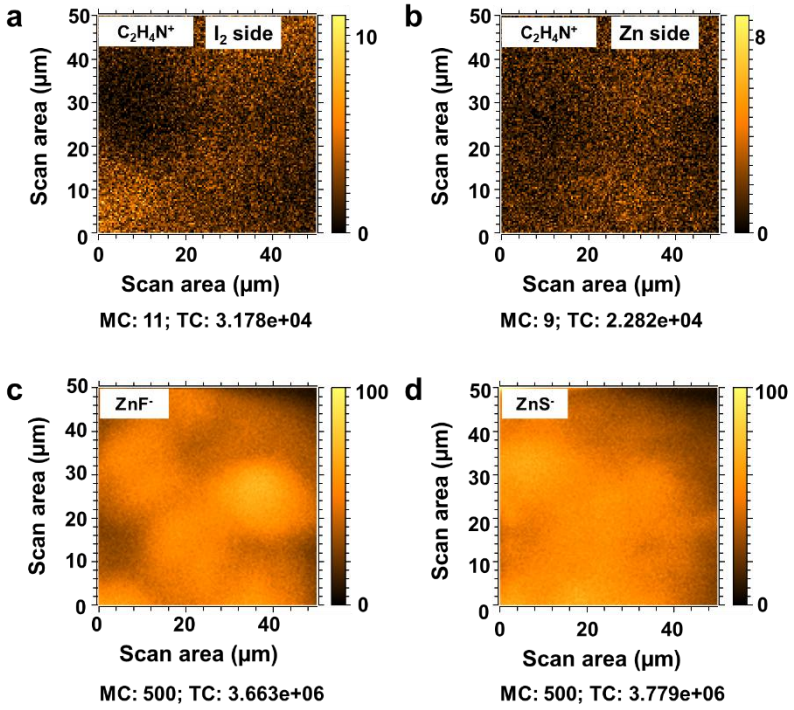

Supplementary Fig. 35 2D element distribution map of characteristic interfacial species at both the I_2 electrode and Zn electrode after cycling with HVOC.

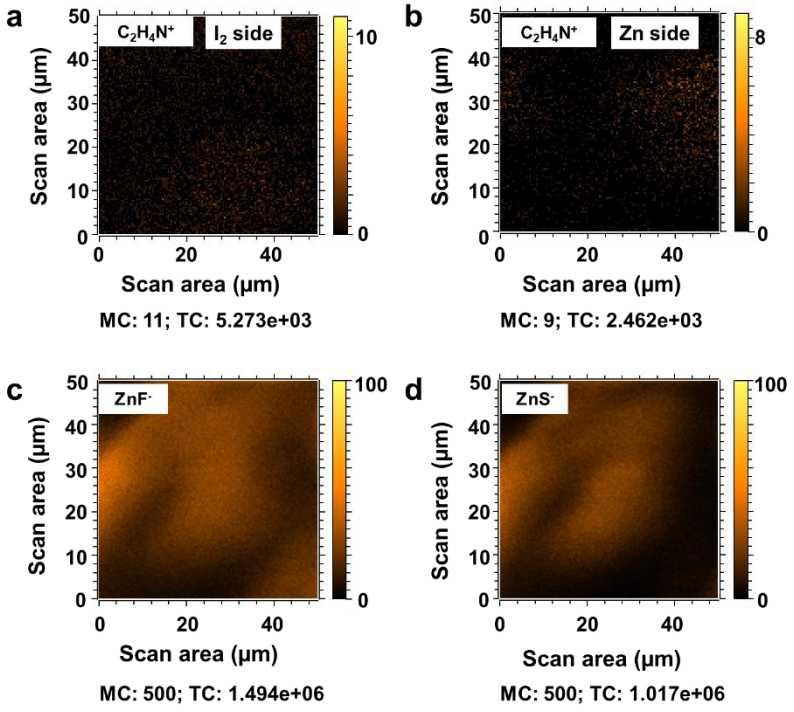

Supplementary Fig. 36 2D element distribution map of characteristic interfacial species at both the I_2 electrode and Zn electrode after cycling with BE.

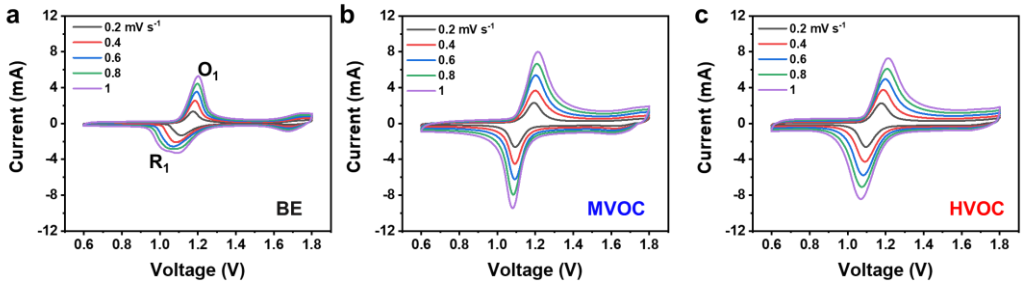

Supplementary Fig. 37 CV curves of Zn||I_2 batteries with **a** BE, **b** MVOC and **c** HVOC at various scan rates.

Supplementary Note 5 To evaluate the reversibility of the iodine redox process, the peak current response was analysed using the Randles–Sevcik relationship[2], which describes the dependence of the peak current i_p on the scan rate:

$$i_p = 0.446\, nFAC^0 \left(\frac{nFD_0}{RT}\right)^{1/2} \nu^{1/2}$$

where n is the number of transferred electrons, A is the electrode surface area, C^0 is the bulk concentration of the redox species, D_0 is the diffusion coefficient, ν is the scan rate, and F , R, and T is the Faraday constant, universal gas constant and temperature, respectively. Under fixed experimental conditions, all parameters except ν are constant, so a reversible redox process is expected to show a linear dependence of i_p on $\nu^{1/2}$. The Linear fitting yields correlation coefficients (R^2) reflects how closely the experimental data follow the Randles–Sevcik prediction. A higher R^2 indicates reduced deviation from the theoretical prediction, suggesting minimal interference from kinetic polarization or irreversible side processes.

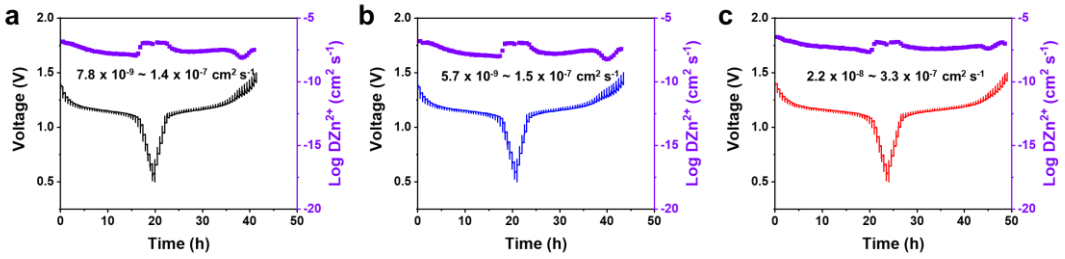

Supplementary Fig. 38 GITT curves and the corresponding Zn^{2+} diffusion coefficients of Zn||I_2 batteries with **a** BE, **b** MVOC, and **c** HVOC.

Supplementary Note 6 Galvanostatic intermittent titration technique (GITT) tests were implemented using a galvanostatic discharge pulse of 60 s at 1 A g^{-1} followed by a 1800 s relaxation time for each step on the Neware battery testing system. Voltage signals were collected with a sampling interval of 1 s during the entire test. The specific Zn^{2+} diffusion coefficients (D_{Zn}) were further caculated based on equation (1):

$$D_{Zn} = \frac{4}{\pi\tau}\left(\frac{n_M V_M}{S}\right)^2\left(\frac{\Delta E_s}{\Delta E_\tau}\right)^2 \quad \text{Equation (1)}$$

Where τ denotes the duration of each current pulse in the GITT measurement, ΔE_s and ΔE_τ correspond to the steady-state voltage variation and the total voltage change during the constant current pulse process, respectively, n_M and V_M represent the molar amount and molar volume of the cathode material, respectively, and S is the geometric area of the electrode.

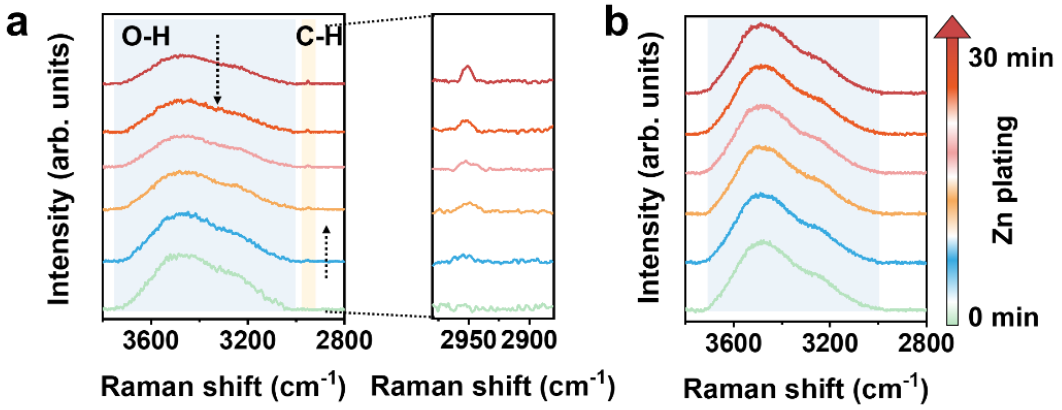

Supplementary Fig. 39 In-situ Raman spectra in the range of 2800-3800 cm^{-1} of the Zn||Zn symmetrical cells with **a** HVOC and **b** BE during Zn plating.

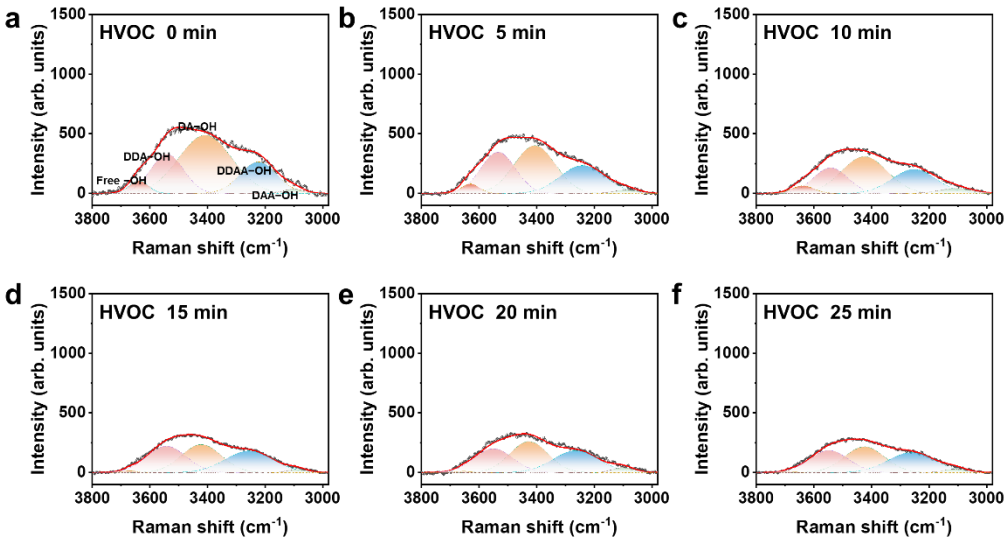

Supplementary Fig. 40 The fitted Raman spectra of the Zn||Zn symmetrical cells with HVOC during Zn plating.

Supplementary Note 7 According to the established proton donor (D)–acceptor (A) mechanism, the O–H stretching band consists of five components: free O–H, DDA–OH, DA–OH, DDAA–OH, and DAA–OH. Among these, free O–H, DDA–OH, and DA–OH represent weak hydrogen bonds (W–H), while DDAA–OH and DAA–OH correspond to strongly hydrogen-bonded (S–H) water[3].

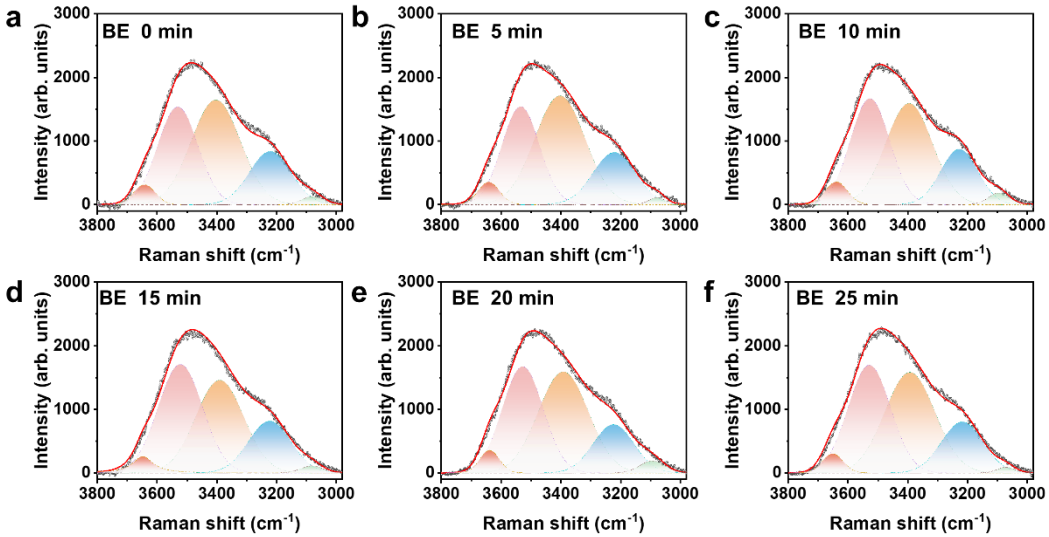

Supplementary Fig. 41 The fitted Raman spectra of the Zn||Zn symmetrical cells with BE during Zn plating.

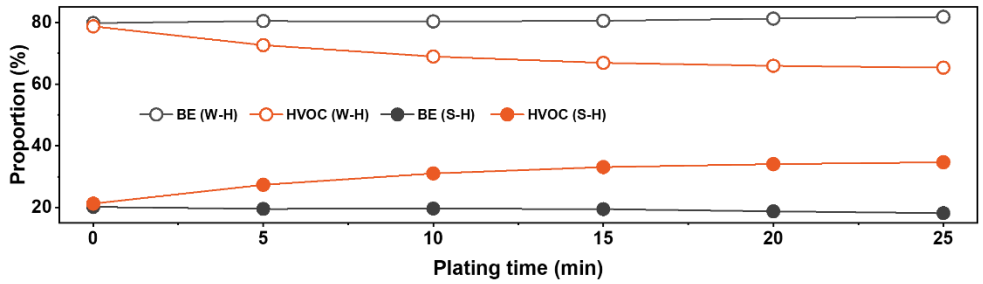

Supplementary Fig. 42 The calculated HBs area ratios.

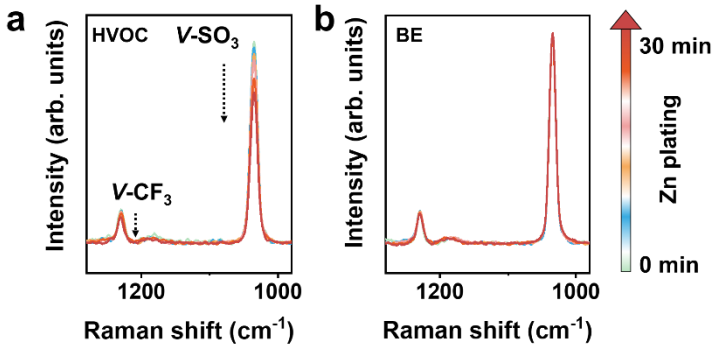

Supplementary Fig. 43 In-situ Raman spectra in the range of 980-1280 cm^{-1} of the Zn||Zn symmetrical cells with **a** HVOC and **b** BE during Zn plating.

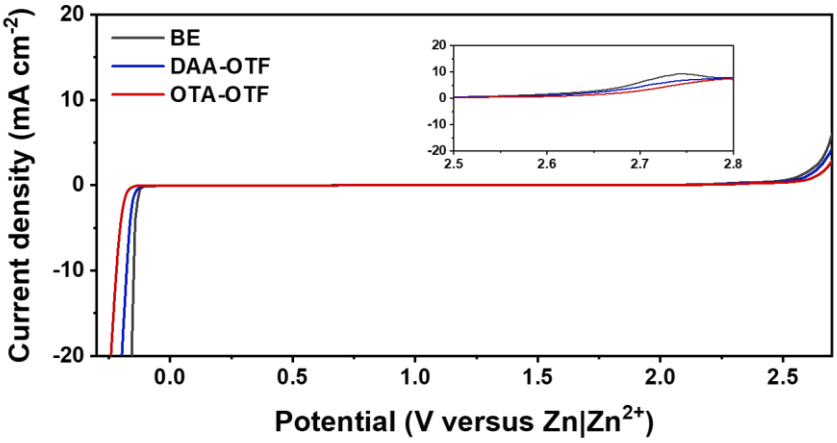

Supplementary Fig. 44 Electrochemical stability window of different electrolytes.

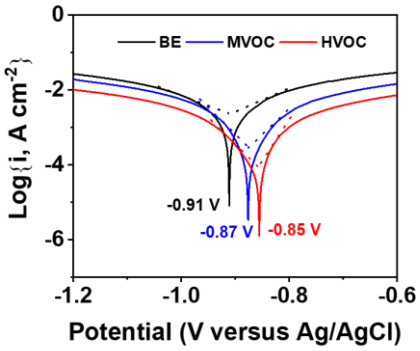

Supplementary Fig. 45 Tafel curves for different electrolytes.

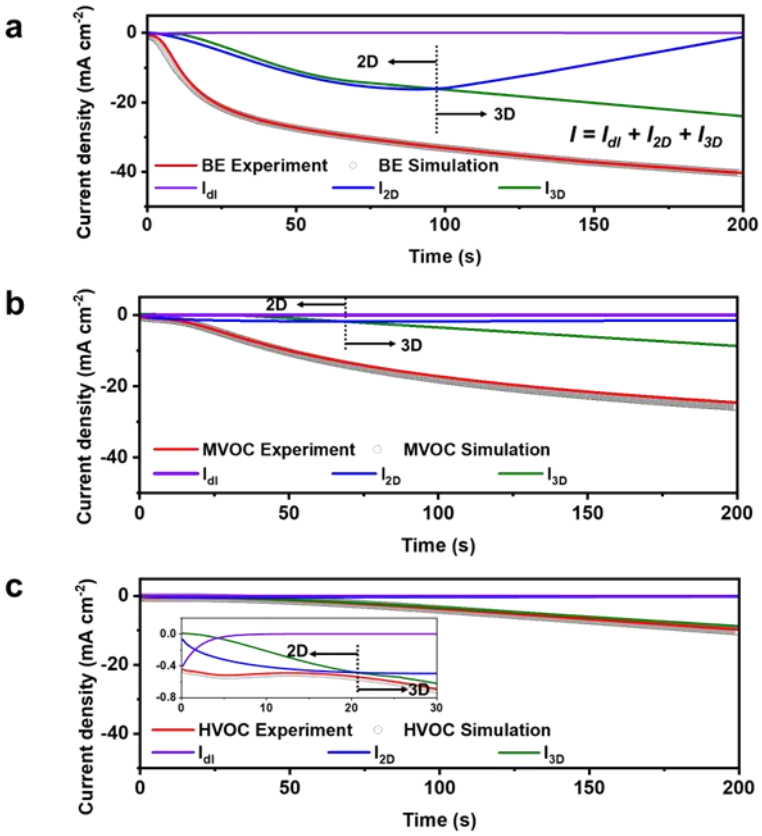

Supplementary Fig. 46 Chronoamperometry (CA) curves and fitted I_{dl}, I_{2D}, and I_{3D} contribution for Zn||Zn cells in **a** BE, **b** MVOC and **c** HVOC.

Supplementary Note 8 To quantitatively distinguish the two-dimensional (2D) diffusion-controlled nucleation stage from the subsequent three-dimensional (3D) growth process, chronoamperometry curves were further analyzed using a multi-component fitting model, following the established methodologies reported in recent literature[4,5]. In the fitting process, we mainly adopted the following equations:

$$I = I_{dl} + I_{dep}$$

$$I_{dl} = I_0 \cdot e^{-\frac{t}{\tau}}$$

$$I_{dep} = I_{2D} + I_{3D}$$

$$I_{2DI}(t) = a_{2DI} \cdot t \cdot \exp\left(-b_{2DI} \cdot t^2\right)$$

$$I_{2DP}(t) = a_{2DP} \cdot t^2 \cdot \exp\left(-b_{2DP} \cdot t^3\right)$$

$$I_{3DI}(t) = c_{3DI} \cdot [1 - \exp\left(-d_{3DI} \cdot t^2\right)$$

$$I_{3DP}(t) = c_{3DP} \cdot [1 - \exp\left(-d_{3DP} \cdot t^3\right)$$

In this analysis, I_{2DI}, I_{2DP}, I_{3DI}, I_{3DP} and I_{dl} correspond to the current contributions from two dimensional instantaneous nucleation, two-dimensional progressive nucleation, three dimensional instantaneous nucleation, three-dimensional progressive nucleation and double layer, respectively. The parameters a, b, c, d, and τ are related describe system-specific physicochemical characteristics.

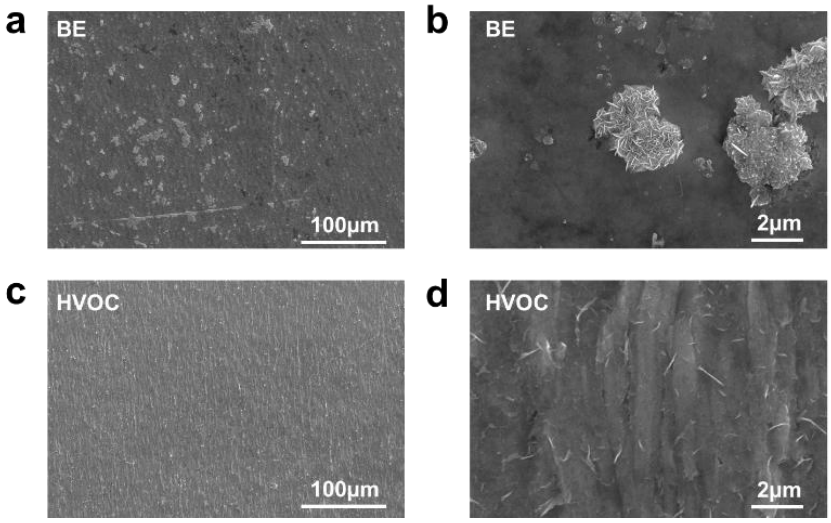

Supplementary Fig. 47 The SEM images for Zn nucleation characterization in **a, b** BE and **c, d** HVOC electrolytes at a current density of 0.05 mA cm^{-2} for 10 min.

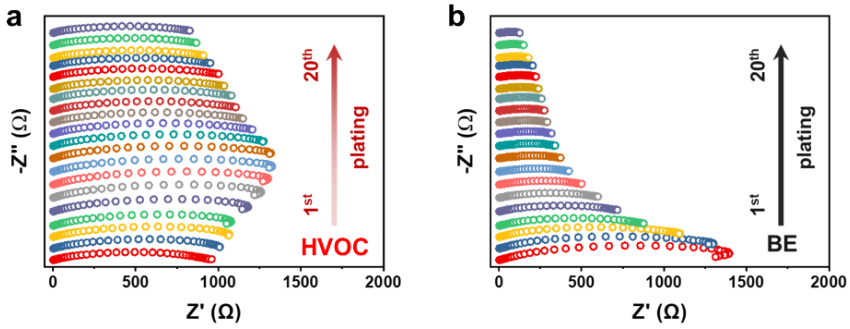

Supplementary Fig. 48 In situ EIS curves of the Zn||Zn cells with **a** HVOC and **b** BE.

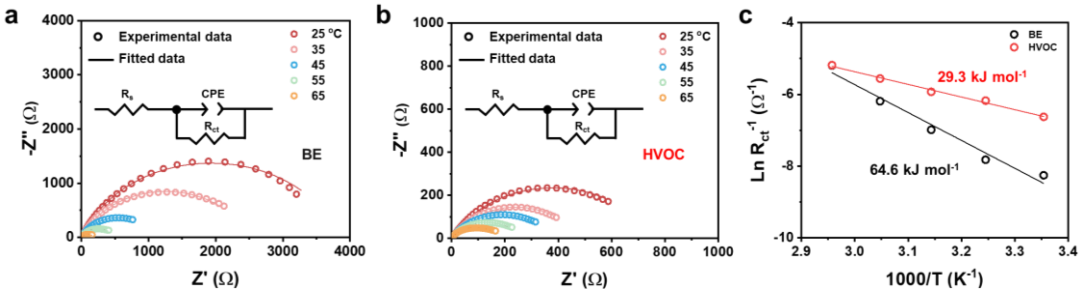

Supplementary Fig. 49 EIS results of Zn||Zn cells with **a** BE and **b** HVOC from 25 to 65 °C. The fitted parameters are provided in Supplementary Tables 1 and 2. **c** The calculated of E_a for different electrolytes.

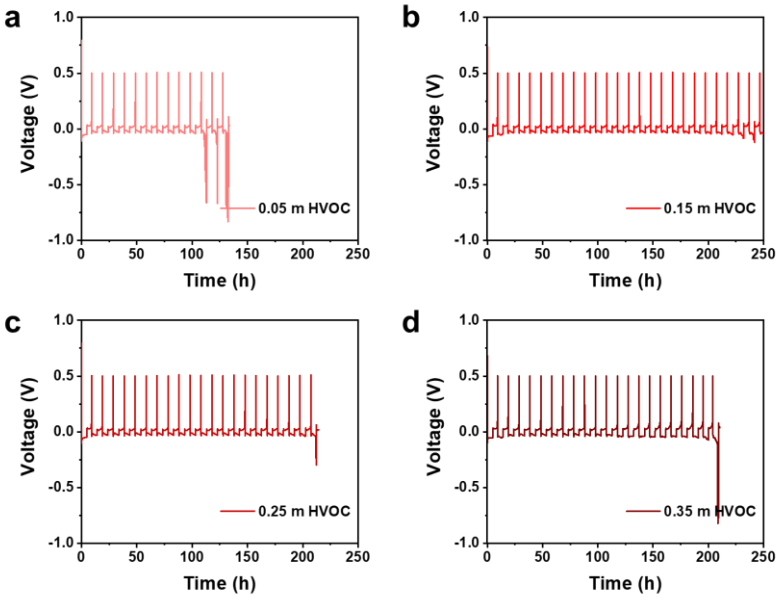

Supplementary Fig. 50 Long-term cycling stability of Zn||Cu cells at 1 mA cm^{-2}, 5 mAh cm^{-2} with **a** 0.05 m HVOC, **b** 0.15 m HVOC, **c** 0.25 m HVOC and **d** 0.35 m HVOC.

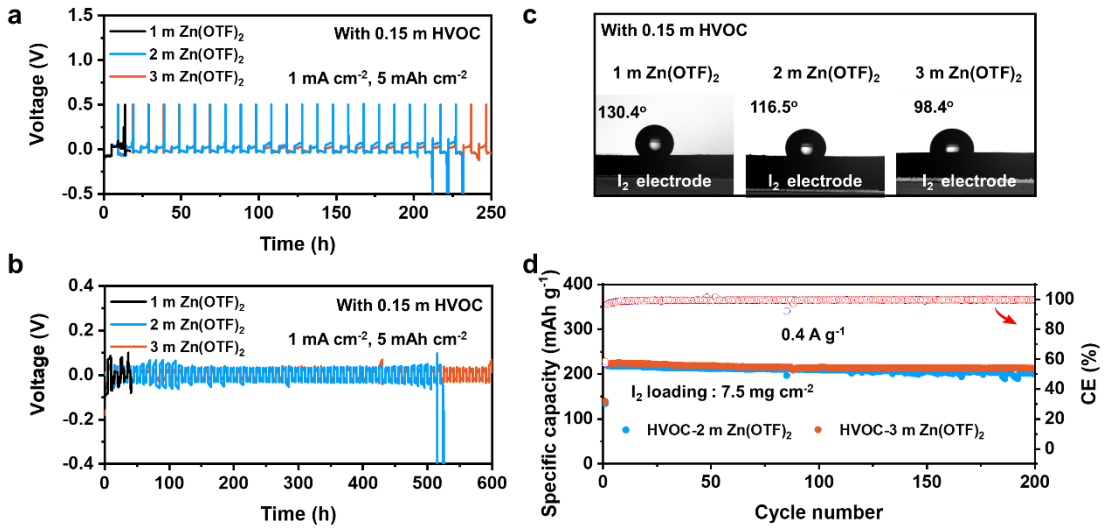

Supplementary Fig. 51 a Long-term cycling stability of Zn||Cu cells at 1 mA cm^{-2}, 5 mAh cm^{-2} with 0.15 m HVOC at different $Zn(OTF)_2$ concentration. **b** Long-term cycling stability of Zn||Cu cells at 1 mA cm^{-2}, 5 mAh cm^{-2} with 0.15 m HVOC at different $Zn(OTF)_2$ concentration. **c** Contact angle of different electrolytes on I_2 electrode surface. **d** Cycling stability of Zn||I_2 battery with HVOC at different $Zn(OTF)_2$ concentrations.

Supplementary Note 9 Zn||Cu and Zn||Zn cells demonstrate stable Zn reversibility in the 2 m and 3 m electrolytes at 1 mA cm^{-2}, 5 mAh cm^{-2}, with the 3 m formulation exhibiting slightly improved performance. In contrast, the 1 m electrolyte shows pronounced initial polarization and cannot sustain stable operation. Contact-angle measurements on the I_2 electrode further reveal that increasing the $Zn(OTF)_2$ concentration enhances surface wettability. Full-cell performance also shows that Zn||I_2 batteries using 2 m and 3 m $Zn(OTF)_2$ exhibit comparable cycling stability, with the 3 m electrolyte providing a marginal advantage. These observations suggest that $Zn(OTF)_2$ concentrations in the range of 2-3 m are suitable for achieving balanced Zn reversibility and positive electrode electrolyte interfacial compatibility.

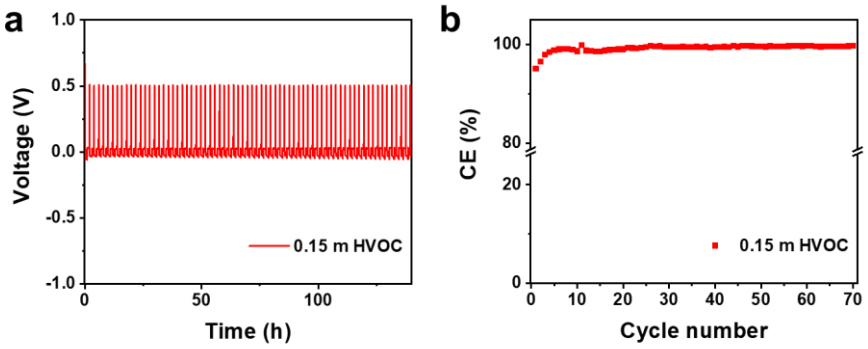

Supplementary Fig. 52 Long-term cycling stability of Zn||Cu cells at 5 mA cm^{-2}, 5 mAh cm^{-2} with 0.15 m HVOC.

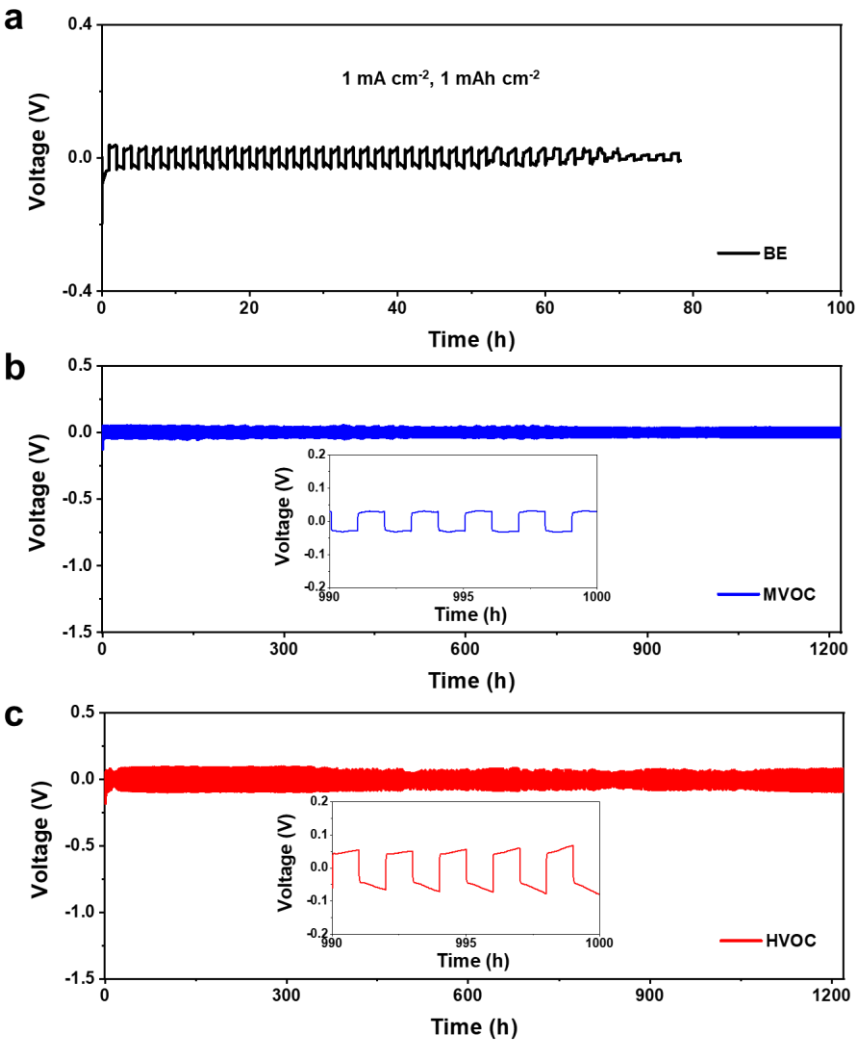

Supplementary Fig. 53 Long-term cycling stability of Zn||Zn cells at 1 mA cm^{-2}, 1 mAh cm^{-2} with **a** BE, **b** MVOC and **c** HVOC.

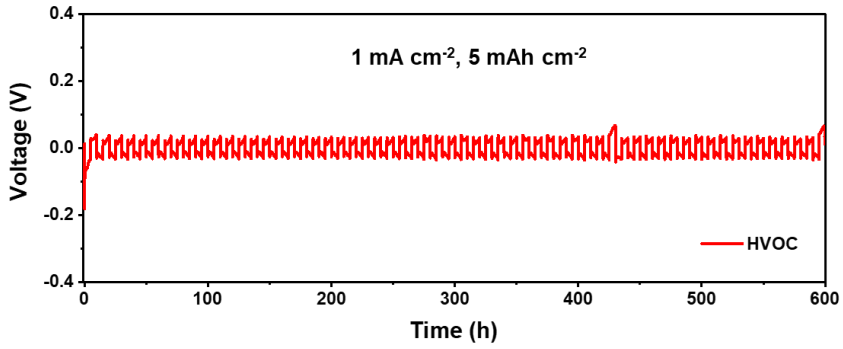

Supplementary Fig. 54 Long-term cycling stability of Zn||Zn cells at 1 mA cm^{-2}, 5 mAh cm^{-2} with HVOC.

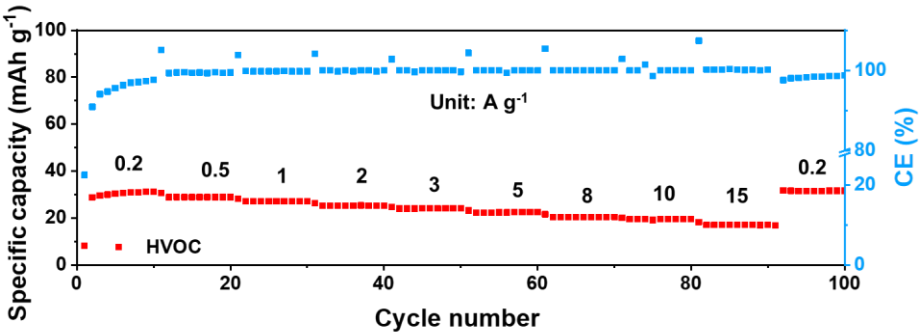

Supplementary Fig. 55 Cycling stability of YP50 electrode with HVOC at various specific current densities.

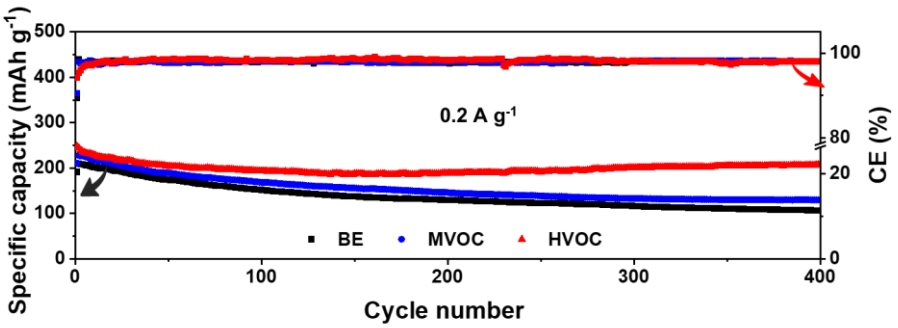

Supplementary Fig. 56 Cycling stability of Zn||I_2 battery with different electrolytes at 0.2 A g^{-1}.

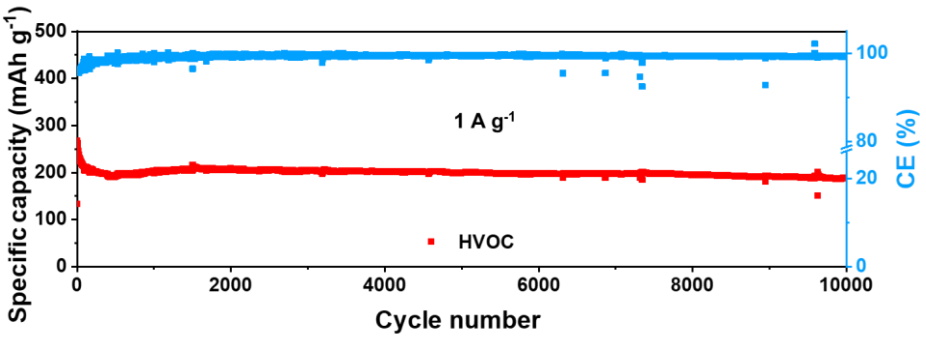

Supplementary Fig. 57 Cycling stability of Zn||I_2 battery with HVOC at 1 A g^{-1}, with an I_2 loading of 1.43 mg cm^{-2}.

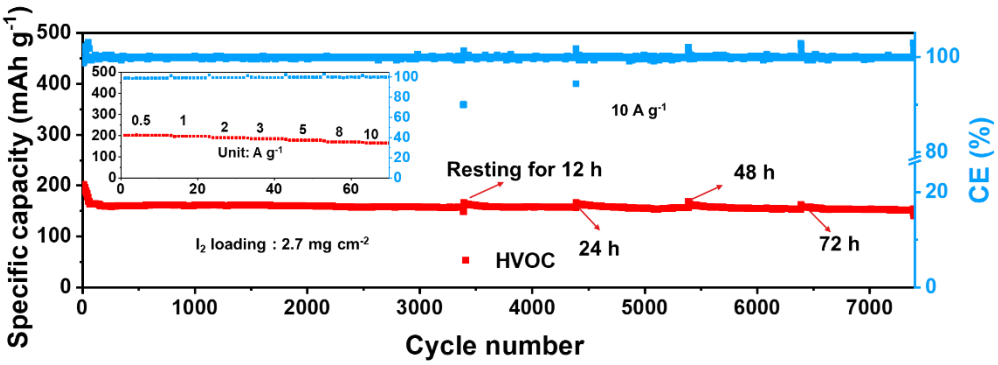

Supplementary Fig. 58 Cycling stability of Zn||I_2 battery with HVOC electrolyte after different resting times at 10 A g^{-1}.

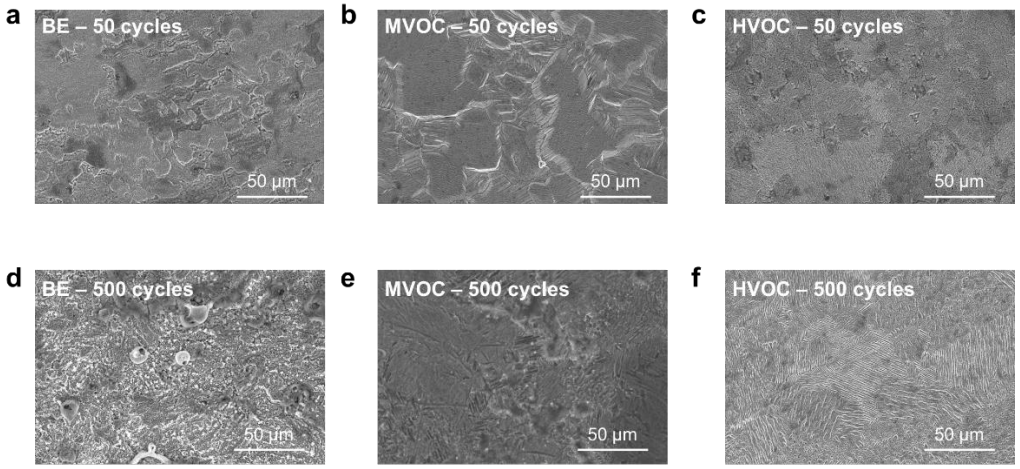

Supplementary Fig. 59 The SEM images of Zn electrode dissembled from Zn||I_2 batteries after 50 cycles with **a** BE, **b** MVOC and **c** HVOC. The SEM images of cycled Zn electrode after 500 cycles with **d** BE, **e** MVOC and **f** HVOC.

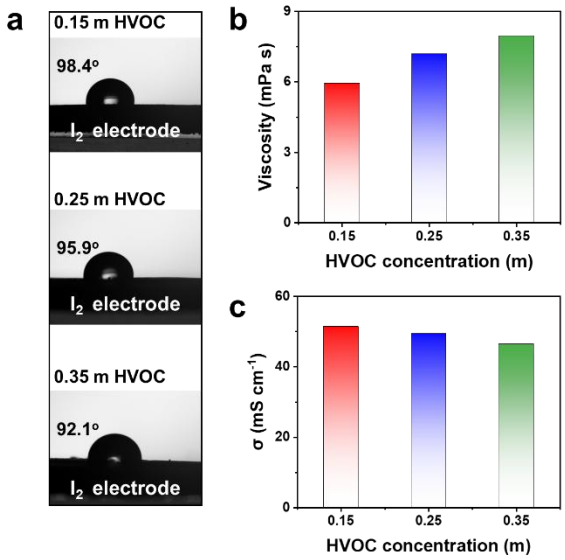

Supplementary Fig. 60 **a** Contact angle of electrolytes with different HVOC concentration on I_2 electrode surface. **b** Viscosities and **c** Ionic conductivities of electrolytes with different HVOC concentrations.

Supplementary Note 10 Contact-angle measurements show that an appropriate amount of HVOC improves wetting of the I_2 electrode, whereas higher HVOC concentrations increase electrolyte viscosity and reduce ionic conductivity.

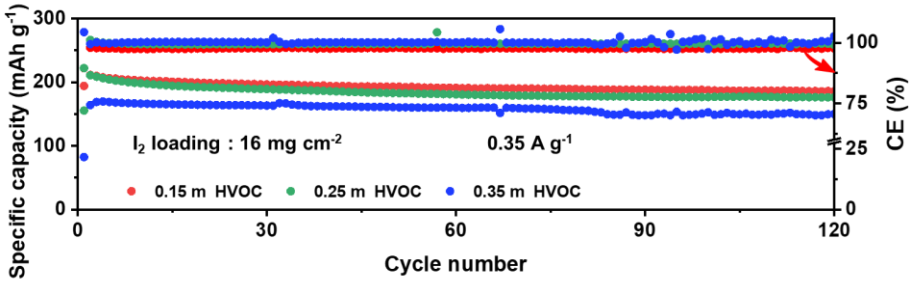

Supplementary Fig. 61 Cycling stability of Zn||I_2 battery using electrolytes with different HVOC concentrations.

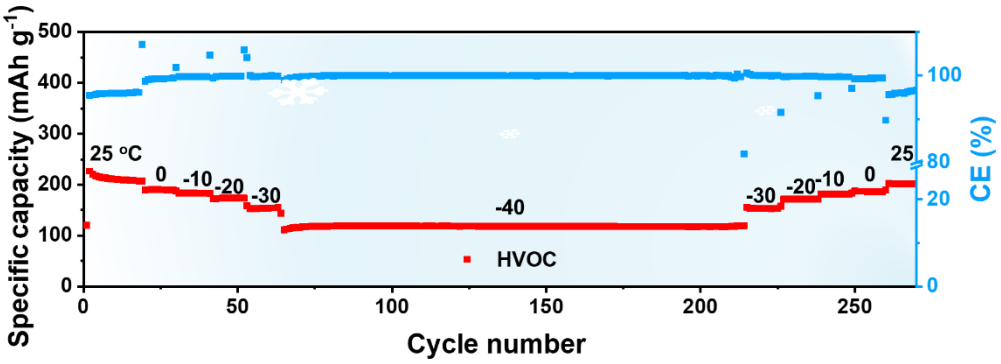

Supplementary Fig. 62 Performance of Zn||I_2 battery with HVOC at 0.2 A g^{-1} from 25 °C to –40 °C.

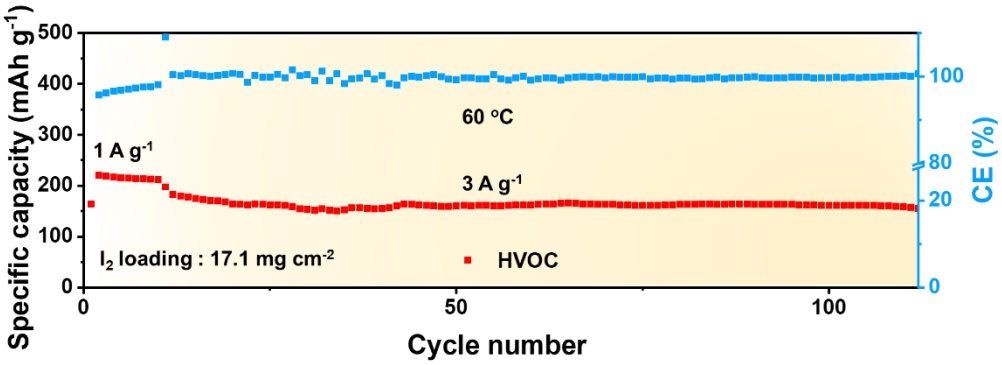

Supplementary Fig. 63 Cycling performance of Zn||I_2 battery with HVOC at 60 °C.

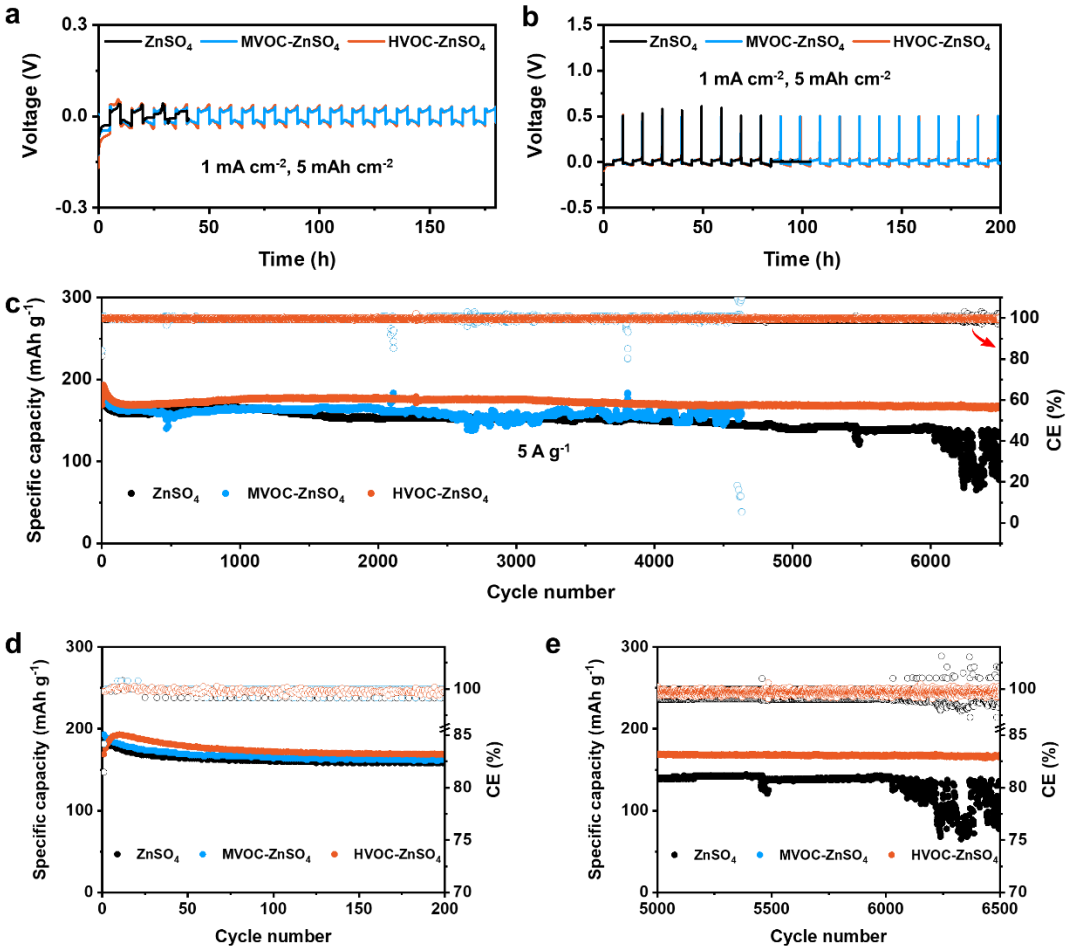

Supplementary Fig. 64 a Long-term cycling stability of Zn||Cu cells at 1 mA cm^{-2}, 5 mAh cm^{-2} with HVOC in $ZnSO_4$-based electrolytes. **b** Long-term cycling stability of Zn||Cu cells at 1 mA cm^{-2}, 5 mAh cm^{-2} with HVOC in $ZnSO_4$-based electrolytes. **c** Cycling stability of Zn||I_2 battery with HVOC in $ZnSO_4$-based electrolytes, with an I_2 loading of 1.3 mg cm^{-2}. **d** Magnified view of the initial cycling region (0–200 cycles) in **c**. **e** Magnified view of the long-term cycling region (5000–6500 cycles) in **c**.

Supplementary Note 11 In the $ZnSO_4$-based electrolytes, at a current density of 1 mA cm^{-2} with an area capacity of 5 mAh cm^{-2}, Zn||Zn and Zn||Cu cells using MVOC- or HVOC-containing $ZnSO_4$-based electrolytes exhibit markedly improved Zn reversibility compared with the $ZnSO_4$. The increased overpotential observed in HVOC-containing $ZnSO_4$-based electrolyte is associated with interfacial electrostatic shielding or competitive adsorption induced by high-valent cations at the Zn surface. In full Zn||I_2 batteries, the HVOC-containing $ZnSO_4$-based electrolyte delivers superior cycling stability and stable Coulombic efficiency (CE), outperforming not only the bare $ZnSO_4$ electrolyte but also the MVOC-containing system.

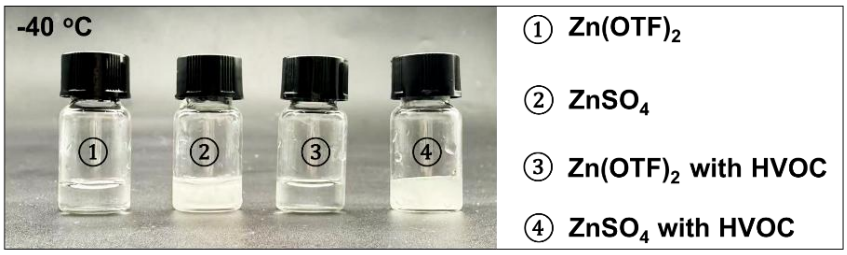

Supplementary Fig. 65 Optical photographs of different electrolytes at −40 °C.

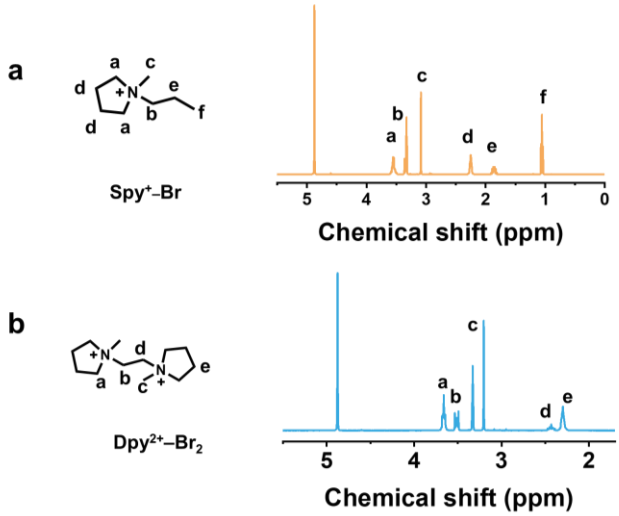

Supplementary Fig. 66 Molecular structures and corresponding ^{1}H NMR spectra of **a** Spy^{+} and **b** Dpy^{2+}.

Supplementary Note 12 We further synthesized a series of structurally related salts with different valence states, following literature procedures[8], namely 1-methyl-1-propyl-pyrrolidinium bromide (Spy^{+}–Br), and 1,1'- (propane-1,3-diyl) bis(1-methyl-pyrrolidinium) bromide (Dpy^{2+}–Br). For the synthesis of Spy^{+}–Br, 1-methylpyrrolidine (4.17 g, 49 mmol) was dissolved in methanol (20 mL), followed by the addition of 1-bromopropane (6.64 g, 54 mmol). The reaction mixture was stirred at 60 °C for 24 h. After completion, the solvent was removed, and the crude product was purified by washing three times with anhydrous ether. Dpy^{2+}–Br was prepared via a similar quaternization route. Briefly, 1-methylpyrrolidine (10 g, 117 mmol) was dissolved in methanol (40 mL), and 1,3-dibromopropane (10.7 g, 53 mmol) was subsequently added. The resulting mixture was heated at 80 °C under stirring for 24 h. After cooling to room temperature, the product was isolated and purified by repeated washing with anhydrous ether. NMR characterization confirms the successful synthesis of the Spy^{+}–Br and

Dpy^{2+}–Br. For $ZnSO_4$-based electrolytes, Spy^{+}–Br and Dpy^{2+}–Br were separately dissolved at a concentration of 0.1 m into 2 m $ZnSO_4$ aqueous solutions. For $Zn(OTF)_2$-based electrolytes, Spy^{+}–Br and Dpy^{2+}–Br were individually added at 0.1 m into 3 m $Zn(OTF)_2$ aqueous solutions to prepare the corresponding electrolytes.

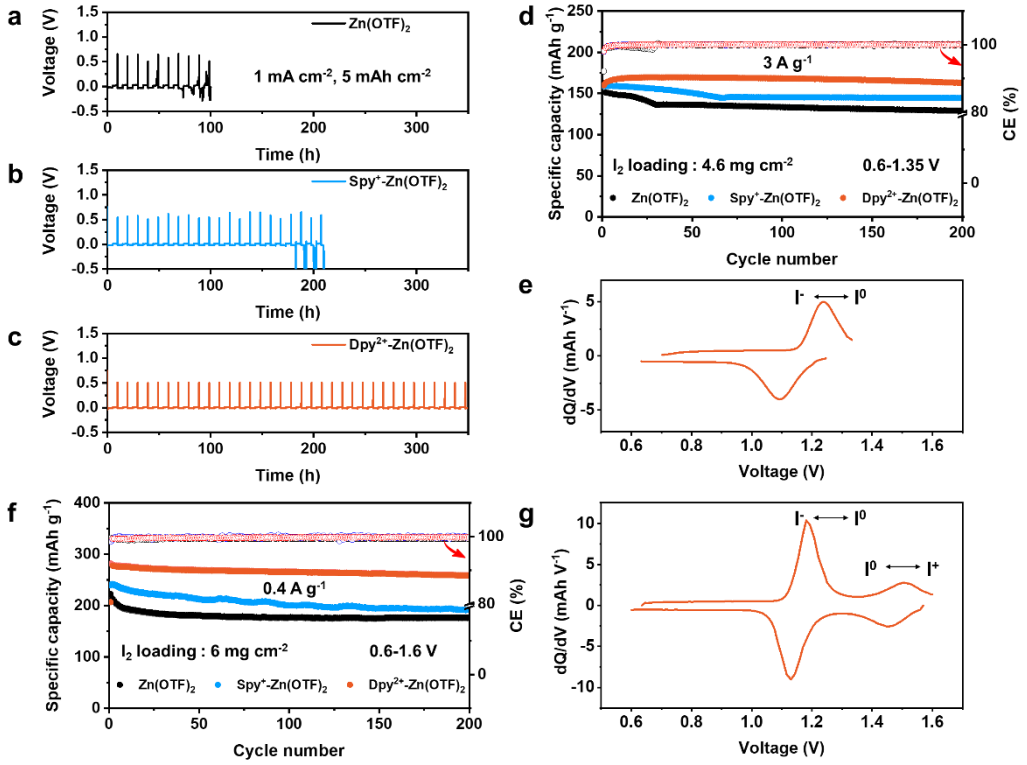

Supplementary Fig. 67 Long-term cycling stability of Zn||Cu cells at 1 mA cm^{-2}, 5 mAh cm^{-2} with **a** $Zn(OTF)_2$, **b** Spy^{+}–$Zn(OTF)_2$, and **c** Dpy^{2+}–$Zn(OTF)_2$. **d** Cycling stability of Zn||I_2 battery with $Zn(OTF)_2$, Spy^{+}–$Zn(OTF)_2$, and Dpy^{2+}–$Zn(OTF)_2$ within 0.6-1.35 V. **e** dQ/dV curves of Zn||I_2 battery with Dpy^{2+}–$Zn(OTF)_2$ within 0.6-1.35 V. **f** Cycling stability of Zn||I_2 battery with $Zn(OTF)_2$, Spy^{+}–$Zn(OTF)_2$, and Dpy^{2+}–$Zn(OTF)_2$ within 0.6-1.6 V. **g** dQ/dV curves of Zn||I_2 battery with Dpy^{2+}–$Zn(OTF)_2$ within 0.6-1.6 V.

Supplementary Note 13 In 3 m $Zn(OTF)_2$ electrolytes with the same additive concentration, Zn||Cu cells were first used to evaluate Zn reversibility. At a current density of 1 mA cm^{-2} and an areal capacity of 5 mAh cm^{-2}, the cycling lifetime of Zn||Cu cells is extended from about 69 h in the bare $Zn(OTF)_2$ electrolyte to 178 h with Spy^{+} and 350 h with Dpy^{2+}, indicating that the higher-valent Dpy^{2+} more effectively stabilizes Zn plating/stripping. We then assembled Zn||I_2 full batteries with an iodine loading of 4.6 mg cm^{-2} and tested at a relatively high specific current density of 3 A g^{-}

[1] for fast screening. A voltage window of 0.6–1.35 V was applied to exclude Br^--induced I^0/I^+ and Br^-/Br^0 redox processes[9,10]. Under these conditions, the Dpy^{2+}-containing electrolyte delivers improved cycling stability, with nearly 100% capacity retention after 200 cycles, compared with 92.8% for Spy^+-containing electrolyte and 86.0% for the bare $Zn(OTF)_2$ electrolyte. The corresponding dQ/dV profiles confirm that only the I^-/I^0 redox couple is involved. It is found that the introduction of Br^- can successfully active I^0/I^+ conversion under a wider voltage window of 0.6–1.6 V. At a relatively low specific current density of 0.4 A g^{-1}, the Dpy^{2+}-based electrolyte retains 92.7% of its capacity after 200 cycles, significantly outperforming Spy^+-containing electrolyte (80.0%) and the bare $Zn(OTF)_2$ electrolyte (79.3%). As shown, Br^- can active higher-valent iodine redox (I^0/I^+), which lead to capacities exceeding the theoretical value for the I^-/I^0 (211 mAh g^{-1}).

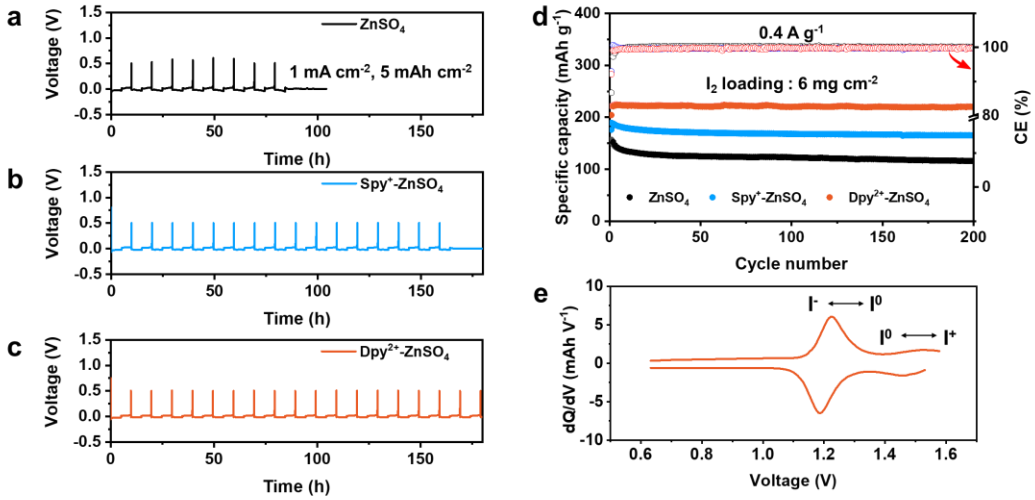

Supplementary Fig. 68 Long-term cycling stability of Zn||Cu cells at 1 mA cm^{-2}, 5 mAh cm^{-2} with **a** $ZnSO_4$, **b** Spy^+–$ZnSO_4$, and **c** Dpy^{2+}–$ZnSO_4$ electrolytes. **d** Cycling stability of Zn||I_2 battery with $ZnSO_4$, Spy^+–$ZnSO_4$, and Dpy^{2+}–$ZnSO_4$ electrolytes within 0.6-1.6 V. **e** dQ/dV curves of Zn||I_2 battery with Dpy^{2+}–$ZnSO_4$ electrolyte within 0.6-1.6 V.

Supplementary Note 14 In $ZnSO_4$ based electrolytes, both Spy^+ and Dpy^{2+} improve Zn reversibility compared with bare $ZnSO_4$, but Dpy^{2+} again provides higher capacity and better cycling stability in Zn||I_2 full cells than Spy^+.

Supplementary Table 1 The parameter of the 0.14 Ah pouch cell.

Positive electrode (I_2)	Length (mm)	55
	Width (mm)	55
	Piece (number)	2
	Areal capacity (mA h cm^{-2})	2.3
	Loading mass (mg cm^{-2})	10.1
Electrolyte (HVOC)	Volume (mL)	~ 2
	Weight (g)	~ 2.3
Separator (GF A)	Length (mm)	60
	Width (mm)	60
	Thickness (mm)	0.25
	Weight (g)	0.25
Negative electrode (Zn Metal)	Length (mm)	55
	Width (mm)	55
	Thickness (μm)	22
	Weight (g)	0.61
	Piece (number)	3
Current collector (Ti mesh)	Length (mm)	55
	Width (mm)	55
	Mesh (number)	100
	Weight (g)	0.80
N/P	8.34	

Supplementary Table 2 Comparison of the Zn||I_2 battery performance based on HVOC in this work with previously reported systems. Note: red and blue shading represent coin and pouch cell configurations, respectively.

Modified strategies	I_2 loading (mg cm^{-2})	Specific current density (A g^{-1})	Cycle number	Capacity retention (%)	Temperature (^oC)	Ref.
HVOC	**7.5**	**0.4**	**1,000**	**84.7**	**25**	***This work***
	16.97	**0.5**	**60**	**100**	**25**	
	22	**0.35**	**250**	**94.3**	**25**	
	17.1	**3**	**100**	**86.1**	**60**	
	10.1	**0.5**	**60**	**96.3**	**25**	
BHEG additive	11	2	3,000	~77	25	11
	21.5	2	2,000	~48.3	25	
BC hydrogel	10.0	0.5 C	280	~100	25	12
	15.3	5 C	4,000	~76.4	25	
	20	1 C	900	~82.9	25	
DDP binder	16.5	6.5 mA cm^{-2}	400	~78.9	25	13
cCNF/AC@ I_2 electrode	14.1	2	3,000	~94.6	25	14
FeHCF/Zn	20.3	8 mA	300	~88.8	25	15
BmBr/ZSO	11.85	0.05	100	95.8	25	16
skin-QSSE	3.2	0.5 C	300	~83.3	25	17
TMAI additive	15	1 mA cm^{-2}	100	91.3	25	18

Supplementary Table 3 Simulated electrolyte compositions.

Electrolyte	Number			
	Zn^{2+}	OTF^-	DAA^+	OTA^{4+}
BE	144	288	-	-
MVOC	144	302	14	-
HVOC	144	344	-	14

Supplementary Table 4. The fitted EIS results for the Zn||Zn cell with BE at different temperatures.

Test temperature (°C)	R_s (Ω)	R_{ct} (Ω)	Error (%)
25	7.54	3850.00	0.80475
35	4.27	2497.00	0.44686
45	4.29	1084.00	0.50866
55	4.71	488.80	0.77279
65	3.95	180.50	1.0982

Supplementary Table 5. The fitted EIS results for the Zn||Zn cell with HVOC at different temperatures.

Test temperature (°C)	R_s (Ω)	R_{ct} (Ω)	Error (%)
25	1.70	755.20	0.67795
35	1.36	481.00	0.49033
45	0.89	376.50	0.38542
55	0.31	259.70	0.83943
65	0.27	178.70	1.3017

Supplementary References

1. Han, X. et al. A fluoride gradient, Zn-salt-rich hydrophobic interphase formed by a zincophilic, hydrophobic, anion-philic polymer “skin” for an anode-free solid Zn battery. *Energy Environ. Sci.* **17**, 9244-9254 (2024).
2. Elgrishi, N. et al. A Practical beginner’s guide to cyclic voltammetry. *J. Chem. Educ.* **95**, 197-206 (2017).
3. Zhang, S. J. et al. Coordination chemistry toward advanced Zn-I_2 batteries with four electron $I^-/I^0/I^+$ conversion. *J. Am. Chem. Soc.* **147**, 16350-16361 (2025).
4. Ouyang, Y. et al. Regulating interfacial molecular configuration to drive facet-selective Zn metal deposition. *Angew. Chem. Int. Ed.* **64**, e202504965 (2025).
5. Zou, Q., Liang, Z., Wang, W., Dong, D. & Lu, Y.-C. A nuclei-rich strategy for highly reversible dendrite-free zinc metal anodes. *Energy Environ. Sci.* **16**, 6026-6034 (2023).
6. Cheng, Y., Jiao, Y. & Wu, P. Manipulating Zn 002 deposition plane with zirconium ion crosslinked hydrogel electrolyte toward dendrite free Zn metal anodes. *Energy Environ. Sci.* **16**, 4561-4571 (2023).
7. Zhao, R. et al. Lanthanum nitrate as aqueous electrolyte additive for favourable zinc metal electrodeposition. *Nat. Commun.* **13**, 3252 (2022).
8. Yu, J. et al. Regulated Li^+ solvation via competitive coordination mechanism of organic cations for high voltage and fast charging lithium metal batteries. *Angew. Chem. Int. Ed.* **64**, e202416092 (2025).
9. Chen, X., Feng, D., Jiao, Y. & Wu, P. Dual-electrode synergistic electrolyte enabling highly reversible multi-electron redox in aqueous zinc-iodine batteries. *Adv. Mater.* **37**, e13389 (2025).
10. Wang, C. et al. Activating and stabilizing a reversible four electron redox reaction of I^-/I^+ for aqueous Zn-iodine battery. *Angew. Chem. Int. Ed.* **63**, e202403187 (2024).
11. Bu, J. et al. Interfacial adsorption layers based on amino acid analogues to enable dual stabilization toward long-life aqueous zinc iodine batteries. *Adv.*

Mater. **37**, e2420221 (2025).

12. Yang, X. et al. High-iodine-loading quasi-solid-state zinc–iodine batteries enabled by a continuous ion-transport network. *Energy Environ. Sci.* **18**, 4730-4739 (2025).
13. Wang, Y. et al. A multifunctional binder for current-collector-free Zn powder anodes. *Adv. Mater.* **37**, e2419702 (2025).
14. Li, Z. et al. Deploying cationic cellulose nanofiber confinement to enable high iodine loadings towards high energy and high-temperature Zn-I_2 battery. *Angew. Chem. Int. Ed.* **63**, e202317652 (2023).
15. Xu, Z. et al. Suppression of interfacial water layer with solid contact using an ultrathin, water-repellent, and Zn^{2+}-selective layer for Ah-level zinc metal batteries. *Energy Environ. Sci.* **18**, 4251-4261 (2025).
16. Lv, Y. et al. Synergistic anion-cation chemistry enables highly stable Zn metal anodes. *J. Am. Chem. Soc.* **147**, 8523-8533 (2025).
17. Cao, S. et al. Skin-like quasi-solid-state electrolytes for spontaneous zinc-ion dehydration toward ultra-stable zinc–iodine batteries. *Energy Environ. Sci.* **18**, 3395-3406 (2025).
18. Kang, J. et al. Dynamic cathode interlayer for ultralow self-discharge and high iodide utilization in zinc-iodine batteries. *Energy Environ. Sci.* **18**, 4800-4810 (2025).